Construction and validation of a bioinformatics-based screen for cuproptosis-related genes and risk model for Alzheimer's disease

RUI HU[1*], ZHEN XIAO[1*], MINGYU QIAO[1], CHAOYU LIU[2], GUIYOU WU[3], YUNYI WANG[1], MINGYOU DONG[2] and ZHONGSHI HUANG[1]

[1]College of Basic Medical Sciences, Youjiang Medical University For Nationalities, Baise, Guangxi 533000, P.R. China; [2]Department of Pathology, Affiliated Hospital of Youjiang Medical University for Nationalities, Baise, Guangxi 533000, P.R. China; [3]School of Pharmacy, Guangxi University of Traditional Chinese Medicine, Nanning, Guangxi 530200, P.R. China

Received June 12, 2024; Accepted August 6, 2024

DOI: 10.3892/mmr.2024.13318

Abstract. The present study aimed to validate the association between core cuproptosis genes (CRGs) and Alzheimer's disease (AD) from both bioinformatics and experimental perspectives and also to develop a risk prediction model. To this end, 78 human-derived temporal back samples were analyzed from GSE109887, and the biological functions of the resulting CRGs were explored by cluster analysis, weighted gene co-expression network analysis and similar methods to identify the best machine model. Moreover, an external dataset GSE33000 and a nomogram were used to validate the model. The mRNA and protein expression of CRGs were validated using the SH-SY5Y cell model and the Sprague-Dawley rat animal model. The RT-qPCR and western blotting results showed that the mRNA and protein expression content of dihydrolipoamide dehydrogenase, ferredoxin 1, glutaminase and pyruvate dehydrogenase E1 subunit β decreased, and the expression of dihydrolipoamide branched chain transacylase E2 increased in AD, which supported the bioinformatic analysis results. The CRG expression alterations affected the aggregation and infiltration of certain immune cells. The present study also confirmed the accuracy and validity of AD diagnostic models and nomograms, and validated the association between five CRGs and AD, indicating a significant difference between patients with AD and healthy individuals. Therefore, CRGs are expected to serve as relevant biomarkers for the diagnosis and prognostic monitoring of AD.

Correspondence to: Professor Zhongshi Huang, College of Basic Medical Sciences, Youjiang Medical University For Nationalities, 98 Chengxiang Road, Baise, Guangxi 533000, P.R. China
E-mail: zhongshihuang@ymun.edu.cn

Professor Mingyou Dong, Department of Pathology, Affiliated Hospital of Youjiang Medical University for Nationalities, 18 Zhongshan Second Road, Baise, Guangxi 533000, P.R. China
E-mail: mydong@ymcn.edu.cn

*Contributed equally

Abbreviations: AD, Alzheimer's disease; Aβ, amyloid β-protein; GEO, Gene Expression Omnibus database; CRGs, core cuproptosis genes; GO, Gene Ontology; KEGG, Kyoto Encyclopedia of Genes and Genomes; GSVA, gene set variation analysis; DLD, dihydrolipoamide dehydrogenase; FDX1, ferredoxin 1; GLS, glutaminase; PDHB, pyruvate dehydrogenase E1 subunit β; DBT, dihydrolipoamide branched chain transacylase E2; $A\beta_{25-35}$, Amyloid β-peptide (25-35); OA, okadaic acid; ROS, reactive oxygen species

Key words: Alzheimer's disease, cuproptosis, immune infiltration, machine learning model, nomogram

Introduction

Alzheimer's disease (AD), a form of dementia, is one of the most prevalent neurodegenerative diseases, which imposes a heavy economic burden on societies around the world (1). The number of people with dementia worldwide is forecast to increase from 57.4 million cases in 2019 to 152.8 million by 2050, according to the latest global dementia data (2). The main pathological symptoms of AD include senile plaques (SP), neurofibrillary tangle (NFTs) and neuronal loss. Numerous studies have explored the pathogenesis of AD and reported that the main pathogenetic mechanisms of AD with important implications for clinical management are amyloid-β (Aβ) protein plaque-associated neurodegeneration, neuronal death and loss of synaptic plasticity, neuroprogenitor degeneration based on NFTs, mitochondrial dysfunction and the gene mutation hypothesis (e.g., mutations in the presenilin 1 and 2 genes can make people more susceptible to AD) (3,4). Due to the association between these pathogenic mechanisms, some researchers have proposed that several mechanisms may be involved in the development of AD (5). One of the major areas of research in this field is to investigate these mechanisms to predict the risk of AD (6). Another area of research is the study of the genome as a predictor of AD risk. It has been shown that the accumulation of dysregulated epigenetic mechanisms during aging may contribute to the development of AD, and it is evident that the genome provides important insights into the molecular mechanisms of AD and is a powerful tool for predicting the risk of the disease (7). Therefore, it is necessary to develop an AD risk prediction model based on the exploration of molecular mechanisms.

Cuproptosis is an essential element that plays an important role in several metabolic processes in the brain (8,9). Excessive cuproptosis in the brain of patients with AD exacerbates oxidative damage and increases the formation of amyloid plaques and NFTs (10,11). The neurotoxic effect of cuproptosis is closely related to the inherent redox properties of Cu^{2+}. Cu^{2+} overload promotes cuproptosis (12), and Cu^{2+} and cuproptosis are closely related to mitochondrial functions (13,14). Cuproptosis, as a newly discovered independent mode of cell death characterized by cuproptosis-dependent and mitochondrial respiratory regulation, can greatly affect mitochondrial functions (15,16). However, numerous studies have concluded that mitochondrial dysfunction-induced oxidative stress and abnormalities in energy metabolism account for a major pathogenic mechanism of AD (17,18). Bioinformatics have recently become increasingly important for exploring the association between cuproptosis and AD, and cuproptosis-related genes (CRGs) are commonly used for immune infiltration analysis and the development of diagnostic models (19). Moreover, nonlinearity, fault tolerance and real-time operation are among the advantages of machine learning algorithms that make them suitable for complex applications (20). Therefore, machine learning tools are widely used in AD exact calculations (21).

There are relatively few studies exploring the potential association between cuproptosis and AD from the perspective of bioinformatics to develop a prognostic risk model. Therefore, the present study aims to investigate the association between CRGs and AD and develop a machine learning-based prognostic risk model for AD. Another objective of the study is to develop a cellular model with okadaic acid (OA)-treated SH-SY5Y cells to validate the expression of the resulting CRGs by the $A\beta_{25-35}$ dementia model in simulated rats to propose a new approach to the diagnosis and prognosis of AD.

Materials and methods

Data collection. The detailed flow chart of the research process is shown in Fig. 1. The gene expression datasets used in the present study are accessible via the Gene Expression Omnibus (GEO) public database (https://www.ncbi.nlm.nih.gov/geo/). This includes the GSE109887 dataset based on the GPL10904 platform, which contains 46 AD samples and 32 control samples (all from human temporal regression samples) (22), and the GSE33000 dataset based on the GPL10558 platform, which contains 310 AD samples and 157 control prefrontal cortex samples (23). A total of 16 CRGs were obtained from the Kyoto Encyclopedia of Genes and Genomes (KEGG) public website (https://www.genome.jp/kegg/) (24).

Differential expression analysis and data processing. Data analysis was performed on the aforementioned datasets in R 4.2.1 (https://www.r-project.org/). The sva R package was used to remove batch effects and the limma R package was employed for differential expression analysis (25,26). All datasets were then normalized in the preprocessCore R package, and differential expression analysis was performed in the limma R package. The threshold for differentially expressed genes (DEGs) was set at |log-fold change (FC)|>1 and $P<0.05$. The screened differential genes were presented using heatmaps and volcano plots, produced using the R packages ggplot2 and pheatmap.

Enrichment analysis of core cuproptosis genes. Gene Ontology (GO) and KEGG pathway analyses were performed on all DEGs as well as five cuproptosis-related hub genes in the ClusterProfiler R package (https://www.bioconductor.org/packages/release/bioc/html/clusterProfiler.html) to identify the relevant pathways and biological functions influenced by DEGs. $P<0.05$ was considered to indicate a statistically significant difference.

Evaluation of immune cell infiltration. The relative abundance of 22 types of immune cells in each sample was estimated based on gene expression data in the CIBERSORT R package (27). The results of the association between CRGs and infiltrating immune cells were presented using the 'ggplot2' R package.

Unsupervised cluster analysis of AD samples. To assess the evolution of AD, the AD samples were divided into several clusters using the K-means algorithm with 1,000 iterations. After which, unsupervised cluster analysis was performed using the ConsensusClusterPlus R package (version 2.60) (https://www.bioconductor.org/packages/release/bioc/html/ConsensusClusterPlus.html).

Weighted gene co-expression network analysis (WGCNA). The WGCNA R package (version 1.72-5; https://cran.r-project.org/web/packages/WGCNA/index.html) was employed to develop co-expression networks and modules in healthy individuals and patients with AD to identify key gene modules associated with AD. The top 50% of genes with the highest variance were applied to subsequent WGCNA analyses to ensure the accuracy of qualitative results. A total of 10 co-expression modules with different colors were obtained using a dynamic cutting algorithm. A heatmap of the topological overlap matrix (TOM) was also presented, in which gene dendrograms and module colors were generated based on gene dissimilarity. The global gene expression profiles in each module were represented by module signature genes. Then an appropriate set of genes for each module was filtered by an algorithm to intersect with the set of differential genes to show the association.

Gene set variation analysis (GSVA). GSVA was performed in the 'GSVA' R package to elucidate the signaling pathways that are differentially enriched between different groups of CRGs (28). The files 'c2.cp. Kegg.v7.4.symbols' and 'c5.go.bp.v7.5.1.symbols' were obtained from the MSigDB web database (https://www.gsea-msigdb.org/gsea/msigdb/index.jsp) for further GSVA analysis. The 'limma' R package was utilized to compare the GSVA scores between different clusters of CRGs to identify the differentially expressed pathways and biological functions.

Nomogram model development and validation. A nomogram model was developed for the clinical diagnosis of AD in the RMS R package (https://hbiostat.org/r/rms/). The 'DALEX' software package (https://modeloriented.github.io/DALEX/) was employed to plot the residual distributions of each model in the test dataset. Each predictor gene received a score based on the level of gene expression for each patient's clinical trait, where the 'total score' represents the sum of the scores of

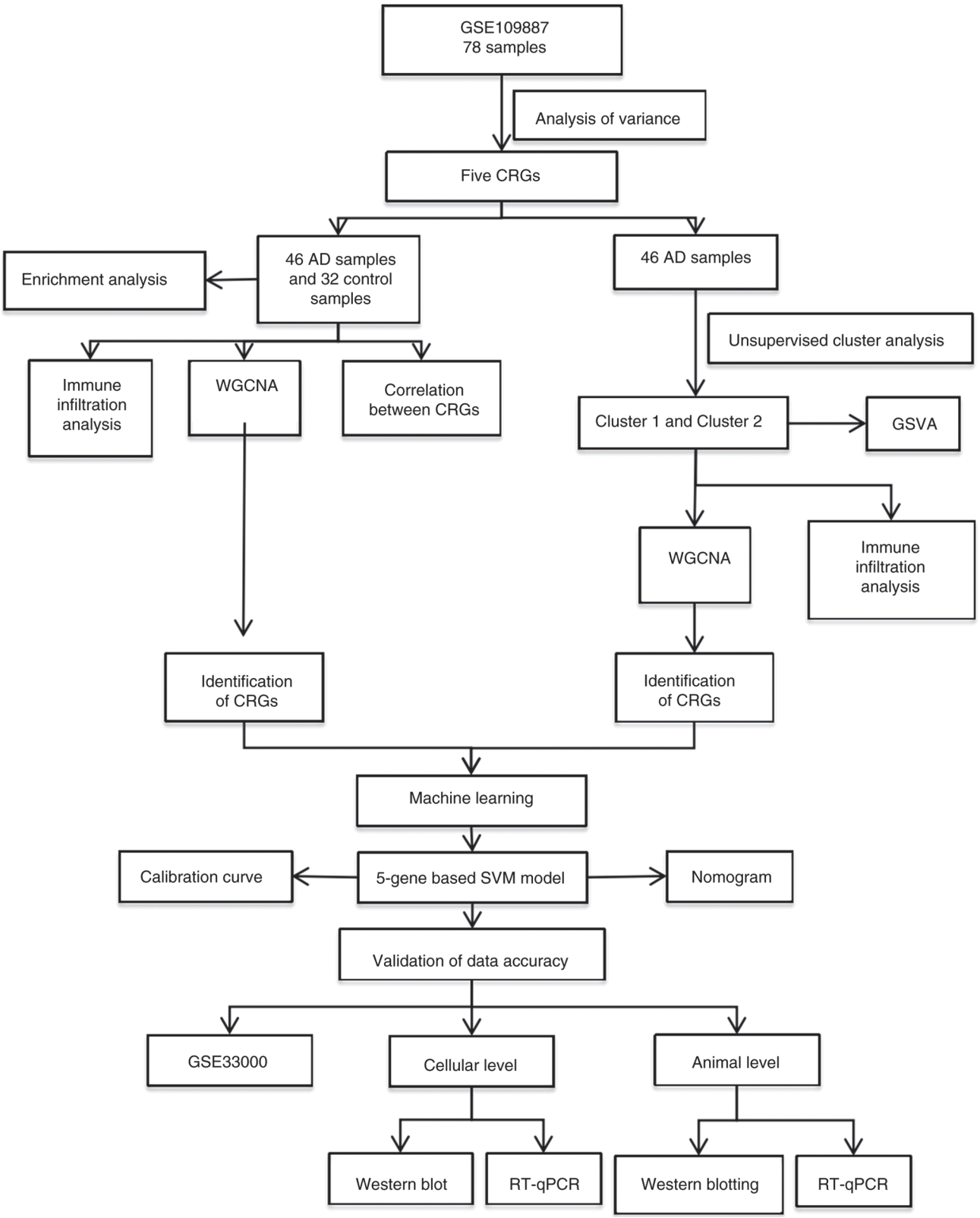

Figure 1. Study flow chart. CRGs, core cuproptosis genes; AD, Alzheimer's disease; GSVA, Gene set variation analysis; WGCNA, weighted gene co-expression network analysis; SVM, Support Vector Machine Model.

the predictors. The risk of disease is assessed based on the score given to each predictive gene, and the sum forms the scoring system. Calibration curves and decision curve analysis (DCA) were used to estimate the predictive power of the nomogram model.

Machine learning and prognostic modeling. Models such as the Random Forest Model (RF), Support Vector Machine Model (SVM), Generalized Linear Model (GLM) and Extreme Gradient Boosting (XGB) were developed using the DEGs of two different clusters of CRGs and the intersecting genes of

AD. The best machine learning model was identified based on the highest ROC values of the aforementioned models. Accordingly, the SVM and the first five important variables were considered the key predictive genes associated with AD. Finally, the diagnostic value of the model was validated by assessing its accuracy based on the GSE33000 dataset.

Animals and the construction of AD models. A total of 30 male Sprague-Dawley rats, (SPF-grade; 8 months old; 220-240 g), were purchased from Beijing Vital River Laboratory Animal Technology Co., Ltd. The rats were housed and given *ad libitum* access to the crop cobalt 60 maintenance rat food diet (Zhiyuan Biomedical Technology Co., Ltd.) and water, modeled, and administered in an SPF-grade laboratory at the Animal Experimentation Center of Youjiang Medical University For Nationalities (Baise, China). The SPF-grade laboratory was equipped with a 12/12 h alternating light and dark barrier system, and its ambient temperature and relative humidity were 25˚C and 60-70%, respectively. Rats were housed until they reached 12 months of age for brain stereotactic injection experiment. The present study received ethical approval for the use of experimental animals from Youjiang Medical University For Nationalities (Baise, China; approval no. 2023040101), and all relevant guidelines were followed throughout the experiment.

The rats were randomly divided into the model, saline and normal control groups (n=10). After weighing, the animals were anesthetized with 2% isoflurane (cat. no. hsc-454-5; Shenzhen Reward Life Technology Co., Ltd.) using a Reward R500 general-purpose small animal anesthesia machine. After which, the rats were placed on a sterile surgical table, and their head was fixed with a stereotaxic apparatus to monitor the respiratory rate. If the respiratory rate remained stable, a stereotaxic injection was performed after the head of the rat was fixed appropriately. Animals in the model group were treated with 1 μl $A\beta_{25-35}$ (Glpbio Technology, Inc.; cat. no. GP10082) on each side of the hippocampus (29,30), whereas those in the saline group were injected with an equal amount of normal saline into each side of the hippocampus. Each rat was administered the injection for a period of 5 min. Following this, the needle was left *in situ* for a further 5 min to prevent the drug from spilling out and evaporating, thereby achieving a less than optimal modelling effect. Those in the normal control group received no surgical treatment. In addition, 100,000 U/g/day of penicillin was injected into each animal for 7 days after surgery to prevent postoperative infections.

Morris water maze (MWM) test. The MWM test was performed using the DigBehv-MG model (Shanghai Jiliang Software Technology Co., Ltd.) (31). The localization and navigation test lasted for 4 days, and each rat was trained 4 times per day. The animals were submerged from the entry point that faced the pool wall, and the time it took to find the platform within 1 min was recorded (escape latency). If a subject failed to find the platform within 1 min, the rat was guided with a glass rod to stand on the platform and remain there for 10 sec to achieve the training purpose; the escape latency for that subject was considered to be 1 min. A total of 2 days after the localization and navigation tests, the platform in the pool was removed and the furthest quadrant of the original platform was taken as the entry point. After which, the rats in each group (the model, saline and normal control groups) were submerged in the water while facing the wall from the entry point, and the escape latency was recorded within 1 min. Moreover, the subjects were submerged in the water from the entry point toward the wall of the pool, and the swimming time and the number of times that the rats crossed the original platform within 1 min were recorded. All subjects were acclimatized overnight before the experiments.

RNA extraction and RT-qPCR to verify the differential expression of CRG mRNA in the AD rat model. On the second day of the MWM test, the animals were anaesthetized [anesthesia was induced at a low concentration (2%) of isoflurane and then increased to a high concentration (5%)] for euthanasia. Prior to euthanasia, it was essential to check the functioning of the gas anesthesia device (Shenzhen Reward Life Technology Co. cat. no. R550IP; Shenzhen Reward Life Technology Co., Ltd.). This was achieved by connecting the system, which consists of the pressure gauge, pressure reducer and controller, to the euthanasia box. The controller power and CO_2 cylinder switch must then be activated. It is essential that no CO_2 is injected into the euthanasia box before the animal is introduced. Once the aforementioned checks were completed, the rats were placed in the euthanasia box. CO_2 was infused into the box at a rate of 30% vol/min until the box was 100% filled with CO_2 for a period of 2 min. Before terminating procedure, it was ensured that the animal was still, not breathing and the pupils were dilated. Once these conditions were met, the CO_2 cylinder was switched off and the animal was observed for a further 11 min. If the animal did not regain consciousness during this period, it was considered to have been successfully euthanized.

The rat hippocampus tissue samples were weighed and stored at -80˚C. To extract RNA from the brain tissue samples, 30 mg of weighed brain tissue samples were taken from each group. After which, centrifuge tubes were filled with the appropriate amount of TRIZOL® reagent (Thermo Fisher Scientific, Inc.; cat. no. 15596026) to extract the total RNA samples based on the mass of the weighed brain tissue samples. The Third Generation Variable Speed Tissue Mill (Tiangen Biotech Co., Ltd.) was used to grind the brain tissue samples in the centrifuge tubes until the brain tissue was completely dissolved in the TRIZOL® reagent. After which, the samples were left on ice for 5 min for subsequent experimentation. RNA was reverse-transcribed into cDNA using the ToloScript All-in-one RT EasyMix for qPCR Kit (cat. no. 22107; Tolo Biotech Co., Ltd.). The results were analyzed in a Light Cycle 96 real-time fluorescence PCR instrument (Roche Applied Science) using the SYBR Green qPCR Mix Kit (cat. no. 22204-1; Tolo Biotech Co., Ltd.). Thermocycling conditions were as follows: Pre-templating at 94˚C for 3 min; followed by 25 cycles at 94˚C for 30 sec, 50˚C for 30 sec and 72˚C for 1 min; and a final extension step at 72˚C for 5 min. The mRNA expression of the genes related to cuproptosis was determined in a Light Cycle 96 real-time fluorescence quantitative PCR instrument (Roche Applied Science). GAPDH was the endogenous control gene, and the primers used for amplification are displayed in Table I. The results were quantified using the $2^{-\Delta\Delta Cq}$ method (32).

Table I. Primer sequences used for RT-qPCR.

Gene name	Primer sequences (5'-3')
GAPDH	F: GACATGCCGCCTGGAGAAAC
GAPDH	R: AGCCCAGGATGCCCTTTAGT
DLD	F: CATTTCAATCGGCTGTCTCA
DLD	R: CAAGCATGTTCCTCCTAGTGTT
GLS	F: CTGAACGAGAAAGTGGAGACCGAA
GLS	R: TGGGCAGAAACCGCCATTAG
PDHB	F: GCATTTGAACTTCCCACAGA
PDHB	R: TTCCCTCCTTAGACAATACAGC
DBT	F: ACGTGTGCTCTGTGGGTTATC
DBT	R: GCTGTCAAACTGAGACACCG
FDX1	F: TGGTGAAACGCTAACGACCA
FDX1	R: CAAGCCAAAGTCCCCTCACA

Protein extraction and western blotting verification of the differential expression of CRGs in a rat model of AD. A total of 50 mg brain tissue was taken from each group. The Third Generation Variable Speed Tissue Mill (Tiangen Biotech Co., Ltd.) was used to grind the brain tissue samples in centrifuge tubes until they were completely dissolved in the RIPA lysis buffer (cat. no. PC101; Epizyme Biotech Co., Ltd.). The samples were then lysed on ice for 30 min, and centrifuged at 12,000 x g for 30 min at 4˚C to remove the supernatant. The steps were performed according to the mass of the sample. The protein concentration was determined by the BCA protein assay. Separation gels were prepared according to the molecular weight of the target protein. The samples were boiled in 4X protein uploading buffer for 5 min and protein samples (20 μg/lane) were separated by SDS-PAGE on 10% gels. The upper gel was electrophoresed at 80 V for 30 min, while the lower gel was electrophoresed at 120 V for 90 min. A current of 250 mA was applied for 80 min for the membrane transfer process. After the transfer was completed, the nitrocellulose membrane was sealed with protein-free rapid closure solution (1X) (cat. no. PS108P; Epizyme Biotech Co., Ltd.) for 20 min at room temperature, and was washed three times with 20X TBS-1% Tween-20 (TBST) buffer (50+950 ml purified water; 10 min/wash). Subsequently, the membrane was incubated overnight at 4˚C with the following primary antibodies: Anti-GAPDH (36 kDa; 1:5,000; Proteintech; cat. no. 0494-1-AP), anti-renal glutaminase A/highly activated glutaminase isoform C [glutaminase (GLS); 65 kDa; 1:5,000; cat. no. 12855-1-AP; Proteintech Group, Inc.], anti-dihydrolipoamide dehydrogenase (DLD; 56 kDa; 1:5,000; cat. no. 16431-1-AP; Proteintech Group, Inc.), anti-pyruvate dehydrogenase E1 subunit β (PDHB; 34 kDa; 1:5,000; cat. no. 14744-1-AP; Proteintech Group, Inc.) and anti-dihydrolipoamide branched chain transacylase E2 (DBT; 53 kDa; 1:3,000; cat. no. 12451-1-AP; Proteintech Group, Inc.). After which, the membrane was washed three times with TBST for 10 min each time. The HRP-conjugated Affinipure Goat Anti-Rabbit IgG(H+L) (cat. no. SA00001-2; Proteintech Group, Inc.) was incubated with the sample at a dilution ratio of 1:5,000 for 1 h at room temperature, and then the sample was washed three times with TBST for 10 min each time. Each membrane was placed in a fully automated chemiluminescence gel imager for color development after 200 μl of the ultrasensitive luminescence solution (A: B formulated at 1:1; Monad Biotech, Co., Ltd.; cat. no. PW30701S) was prepared. GAPDH was selected as the endogenous control protein. Western blot semi-quantification was performed using ImageJ (v. 1.54d; National Institutes of Health).

STR identification statement for SH-SY5Y cells. The genomic DNA of the SH-SY5Y cell line was sequenced, and the STR results showed good typing results for the cell line. Furthermore, no cross contamination of human cells was found in this cell line as seen in the STR typing results. Moreover, the DNA typing result of this cell line 100% matched with the cell typing result of SH-SY5Y in the cell bank.

Cell culture and AD model development. SH-SY5Y cells were purchased from Wuhan Pronocell Life Science Technology Co., Ltd., and OA for AD cell modelling was purchased from MedChemExpress (cat. no. 209266-80-8) (33). SH-SY5Y cells were incubated in a cell culture containing 5% CO_2 at 37˚C. The complete medium used for the culture of the cells was a combination of Dulbecco Modified Eagle medium with F-12 (Gibco; Thermo Fisher Scientific, Inc.), 14% Sigma Australia Fetal Bovine Serum (Sigma-Aldrich; Merck KGaA) and a 1% penicillin-streptomycin (Beijing Solarbio Science & Technology Co., Ltd.) solution mixture. The cells in the control group were cultured to 85-90% density in complete medium without drugs and then used for experiments. The cells in the DMSO group were first cultured to 85-90% density in complete medium without drugs, and then cultured in complete medium containing a low concentration of DMSO [consistent with the concentration of DMSO contained in the AD group (0.000625% DMSO/ml of medium)] for 24 h and then used for experiments. The cells in the AD group were first cultured to 85-90% density in complete medium without drugs, and then cultured in complete medium containing OA concentration of 25 nM for 24 h and then used for experiments. The OA was dissolved with DMSO to formulate 40 μmol/l OA mother liquor, and 20 μl OA mother liquor was taken and mixed with 180 μl 10% DMSO (diluted in enzyme-free sterile water) to formulate 4 μmol/l OA working solution, which was stored at 4˚C. Using the aforementioned complete medium, SH-SY5Y cells were diluted to a density of $1x10^5$ ml and 200 μl/well cell suspension was inoculated in 96-well plates. Each well received a full medium supplemented with OA solutions at concentrations of 0, 10, 20, 40 and 80 nmol/l after 24 h at 37˚C and 5% CO_2, and there were four replicates for each concentration.

To compare the effects of different OA concentrations on the proliferation of SH-SY5Y cells after 24 h, CCK-8 reagent (20 μl; cat. no. C6005M; Suzhou Youyi Landi Biotechnology Co., Ltd.) was added to each well and incubated for 2 h in 5% CO_2 at 37˚C. The absorbance values at 450 nm were measured using a BIOBASE-EL10A enzyme marker (BIOBASE Group) (34). The experiment was conducted three times, and the optimal drug concentration of 25 nM for OA-induced AD in the cell model was found by monitoring the cell growth under a fluorescence microscope and calculating the

Table II. Primer sequence for RT-qPCR.

Gene names	Primer sequences (5'-3')
GAPDH	F: GAAGGCTGGGGCTCATTT
GAPDH	R: CAGGAGGCATTGCTGATGAT
DLD	F: GTGATTTACACACACCCTGA
DLD	R: GTCTGTCGATTTCTGCCCAA
GLS	F: CTGAGCCCTGAAGCAGTTCG
GLS	R: AGGAGACCAGCACATCATACCC
PDHB	F: GTGTCTGGCTTGGTGCGGAG
PDHB	R: ACCTTGTATGCCCCATCATACTG
DBT	F: CCATTGCATTTGCTCGTGGA
DBT	R: ACCCTGCTCAGTATCCATTGC
FDX1	F: CTTGTTCAACCTGTCACCTCATCT
FDX1	R: CAGCCACTGTTTCAGGCACTC

absorbance values. The viability of cells in response to an optimal OA concentration of 25 nM was also measured using the CCK-8 assay. First, the cells were seeded into a 96-well plate and incubated for 24 h, after which, the medium was changed in each well (one group was treated with complete medium only and the other was treated with complete medium containing 25 nM OA) for 24 h. Subsequently, the cells were incubated with CCK-8 reagent for 2 h. The experimental incubation conditions were all performed in an atmosphere containing 5% CO_2 at 37˚C. This assay was repeated three times in four replicates.

RNA extraction and RT-qPCR to verify the differential expression of CRG mRNA in SH-SY5Y cells. Total RNA samples were extracted by adding TRIZOL® reagent to the cell samples of the model group, which were induced with 25 nM of OA, cell samples from the DMSO group cultured with the same concentration of DMSO as OA in the model group, and cell samples of the control group, which received no treatment. The subsequent RT-qPCR protocol was the same as aforementioned in the animal studies. GAPDH was selected as the endogenous control gene, and the primers used for amplification are displayed in Table II.

Protein extraction and western blotting verification of differential expression of CRGs in SH-SY5Y cells. Western blotting was performed to assess the expression of proteins in different groups of cells (control group and AD group), with GAPDH as the endogenous reference protein. The culture flasks were washed with pre-cooled PBS, the cells were collected using a cell spatula and centrifuged in a 15-ml tube at 1,200 rpm for 5 min. The centrifuge tube was filled with RIPA lysis buffer, protein phosphatase inhibitor mixture and protease inhibitor (100:1:1) and lysed on ice for 30 min. The subsequent western blotting protocol was the same as aforementioned in the animal studies.

Statistical analysis. The data were processed and statistically analyzed in R software version 4.2.1, ImageJ 1.54d, SPSS version 25 (IBM Corporation), and GraphPad Prism version 9.0 (Dotmatics). Unpaired Student's t-test was used to determine the differences between the two experimental groups, whereas one- or two-way analyses of variance (ANOVA) were used to compare differences between three or more groups. Tukey's post hoc test was used after one-way ANOVA and Bonferroni post hoc test was used after two-way ANOVA. All data were presented as mean ± SD. $P<0.05$ was considered a indicate a statistically significant difference.

Results

Identification of DEGs. The present study analyzed gene expression array data from 78 human-derived temporal regression samples from the GEO database. Fig. 2A presents a volcano plot showing the 78 DEGs after screening, including one upregulated and four downregulated expressed genes (Fig. 2B). Fig. 2C shows a heatmap of the five differentially expressed related genes. Characterized genes were screened by differential expression analysis.

Biological function analysis of cuproptosis-related core genes. The obtained differentially expressed CRGs underwent GO analysis. Regarding biological processes, the differentially expressed CRGs were mainly enriched in the 'cellular amino acid catabolic process', while the cellular components they were mainly enriched in were the 'mitochondrial matrix' and 'oxidoreductase complex'. In terms of molecular function, the differentially expressed CRGs were enriched in the 'oxidoreductase activity, acting on the aldehyde or oxo group of donors, NAD or NADP as acceptor' and 'oxidoreductase activity, acting on the aldehyde or oxo group of donors' (Fig. 3A). According to the KEGG enrichment analysis, the differentially expressed CRGs were mainly involved in 'lipoic acid metabolism', 'citrate cycle (TCA cycle)', 'propanoate metabolism', 'pyruvate metabolism', 'valine, leucine and isoleucine degradation', 'glycolysis/gluconeogenesis' and 'carbon metabolism' (Fig. 3B).

Correlation analysis of cuproptosis-related core genes. Subsequently, enrichment and correlation analyses were performed on the obtained CRGs to explore whether they play a relevant role in the development of AD. The results of the enrichment analysis, GO analysis and KEGG analysis indicated that several genes, such as PDHB and DLD, showed synergistic effects, but DBT and the remaining four genes showed significant antagonistic effects (Fig. 3C). In addition, further investigation of the correlation patterns of these CRGs revealed that both DBT and DLD were significantly correlated with other modulators (Fig. 3D).

Immune infiltration cell analysis of cuproptosis-related core genes. Immune infiltration analysis was performed based on the CIBERSORT algorithm, and the results showed differences between patients with AD and healthy individuals in the proportion of 22 infiltrating immune cell types. The heatmap shows the distribution of the 22 infiltrating immune cell types (Fig. 4A). The results showed that patients with AD had higher levels of immune infiltration of naive B cells, CD8 T cells, resting natural killer (NK) cells, monocytes, M1 macrophages, resting mast cells, eosinophils and neutrophils compared with

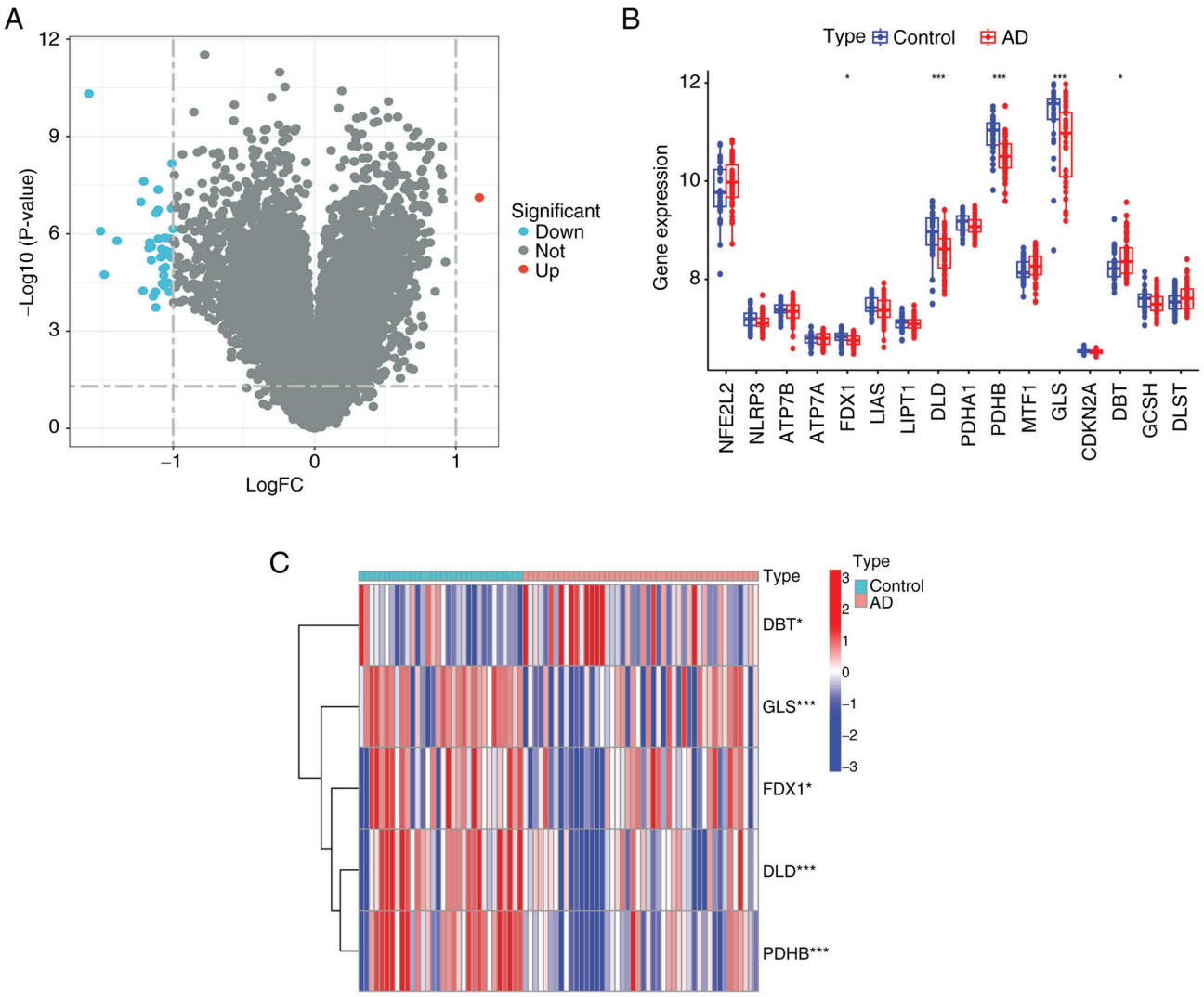

Figure 2. Identification of CRGs dysregulated in AD. (A) Volcano plot of 78 DEG expressions, with significantly upregulated genes in red and downregulated genes in green. (B) Box plot showing the expression of 13 CRGs between AD and non-AD controls. (C) Heatmap presenting the expression of 5 CRGs. *P<0.05 and ***P<0.001. CRGs, core cuproptosis genes; AD, Alzheimer's disease; DEGs, differentially expressed genes.

in the control patients. By contrast, plasma cells, CD4 memory resting T cells, follicular helper T cells, activated NK cells, M0 macrophages, M2 macrophages and activated dendritic cells exhibited lower infiltration levels in patients with AD (Fig. 4B). The correlation between the five differentially expressed CRGs and infiltrating immune cells demonstrated that DLD was positively correlated with dendritic-activated cells, M2 macrophages and mast-activated monocytes. Moreover, GLS showed a positive correlation with dendritic-activated cells (Fig. 4C). These results suggest that CRGs may be a key factor in regulating the molecular and immune infiltration status in patients with AD.

Characterization of epithelial cell aggregation in patients with AD. To elucidate the expression patterns associated with cuproptosis in AD, 78 samples were grouped based on the expression profiles of the five CRGs using a consistent clustering algorithm. The number of clusters was most stable when the k-value was set to 2 (k=2) and the cumulative distribution function (CDF) curves fluctuated within the smallest range of the common index (0.2-0.6; Fig. 5A). When the k-value was 2-9, the area under the CDF curve exhibited a difference between the two CDF curves (k and k-I; Fig. 5B). Clustering the k-values ranging 2-9 showed a concordance score of >0.9 across subtypes only when the k-value was equal to 2 (Fig. 5C). The results show that the consistency scoring of each subtype is satisfied only for k=2.

Characterization of differentiation and immune infiltration of regulatory factors in two clusters of cuproptosis. Combined with the heatmap of the shared matrix, 78 patients with AD were grouped into two clusters, including cluster 1 (n=46) and cluster 2 (n=32). To compare the molecular features of the clusters, the expression differences of the five CRGs between cluster 1 and 2 were first assessed (Fig. 6A). Different expression profiles of CRGs were observed between the two cuproptosis intoxication patterns, with cluster 1 exhibiting high expression levels of DBT and cluster 2 characterized by increased expression of DLD, FDX1, GLS and PDHB (Fig. 6B). The immune infiltration analysis revealed a difference between the clusters in the immune infiltration profile (Fig. 6C). The percentage of macrophage M1 was higher in cluster 1, whereas

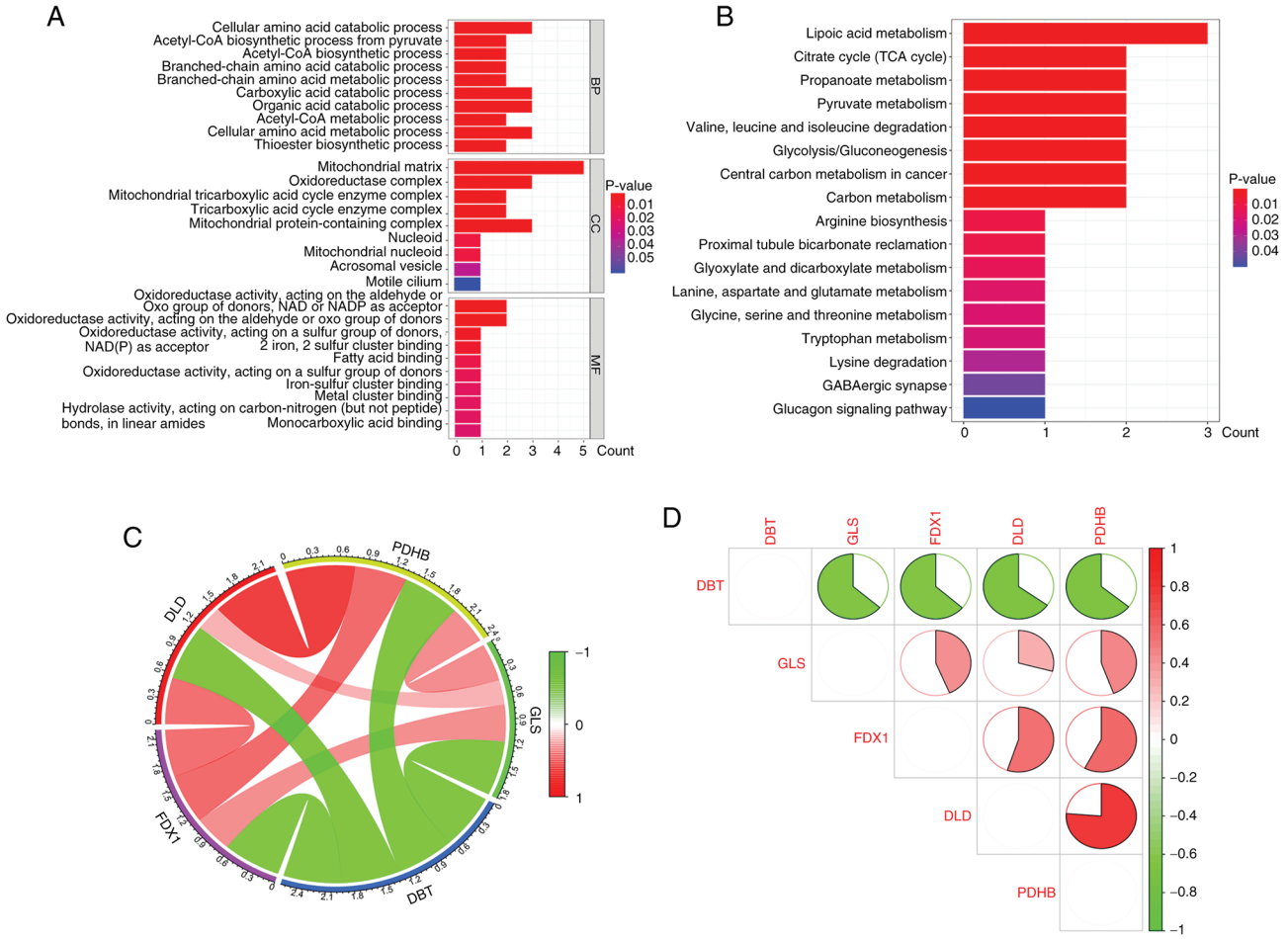

Figure 3. GO and KEGG pathway enrichment analysis and correlation analysis of CRGs in AD. (A) Results of GO enrichment analysis of CRGs are shown by bar graph display. (B) KEGG pathway enrichment results are shown as bar graphs. (C) Pie chart of gene correlation of five CRGs. (D) Correlation analysis of the five differentially expressed CRGs. Green and red colors indicate negative and positive correlations, respectively. Correlation coefficients are labeled with the area of pie charts. GO, Gene Ontology; KEGG, Kyoto Encyclopedia of Genes and Genomes; CRG, core cuproptosis genes; DLD, dihydrolipoamide dehydrogenase; FDX1, ferredoxin 1; GLS, glutaminase; PDHB, pyruvate dehydrogenase E1 subunit β; DBT, dihydrolipoamide branched chain transacylase E2; AD, Alzheimer's disease.

the percentage of dendritic activated cells was higher in cluster 2 (Fig. 6D). The results showed that the correlation between CRGs and immune cells was also increased after splitting into two clusters.

Development of a co-expression networks. The WGCNA algorithm was used to develop co-expression networks and modules in healthy individuals and patients with AD to identify key gene modules associated with AD. After calculating the variance of each gene expression in GSE109887, the top 25% of genes with the highest variance were selected for further analysis. Co-expressed gene modules were identified when the value of soft power was set to 11 and the scale-free R2 was equal to 0.5 (Fig. 7A). A total of 10 gene modules with different colors were obtained using the dynamic cutting algorithm, and then a heatmap of the TOM was created (Fig. 7B-D). These genes were then used in each of the ten color modules in turn to examine the degree of similarity and proximity of module-clinical feature co-expression in the control and AD groups. By analyzing the similarity and adjacency of the co-expression of the clinical features of the module (control and AD), it was found that the turquoise module had the strongest relationship with AD, and had a strong correlation with AD with $P=4e^{-06}$ in the AD group (Fig. 7E). In addition, a positive association was observed between the turquoise module and module-associated genes (Fig. 7F).

A similar approach was also employed to further analyze the DEGs between the two cuproptosis clusters. β=19 and R2=0.8 were screened as the most suitable soft threshold parameters for developing the scale-free network (Fig. 8A). The heatmaps demonstrated the TOM of all module-related genes (Fig. 8B-D). An analysis of the relationship between modules and clinical features (clusters 1 and 2) revealed a strong correlation between turquoise modules and AD clusters (Fig. 8E). The correlation analysis also showed a significant association between the turquoise module genes and selected modules (Fig. 8F).

Identification of specific genes and GSEA. A total of 134 related genes were identified by analyzing the crossover between the modular genes associated with AD (Fig. 9A). GSVA analysis was used to further investigate the functional differences between the two clusters in terms of cluster-specific DEGs. Cluster 1 was found to be enhanced in non-small cell lung

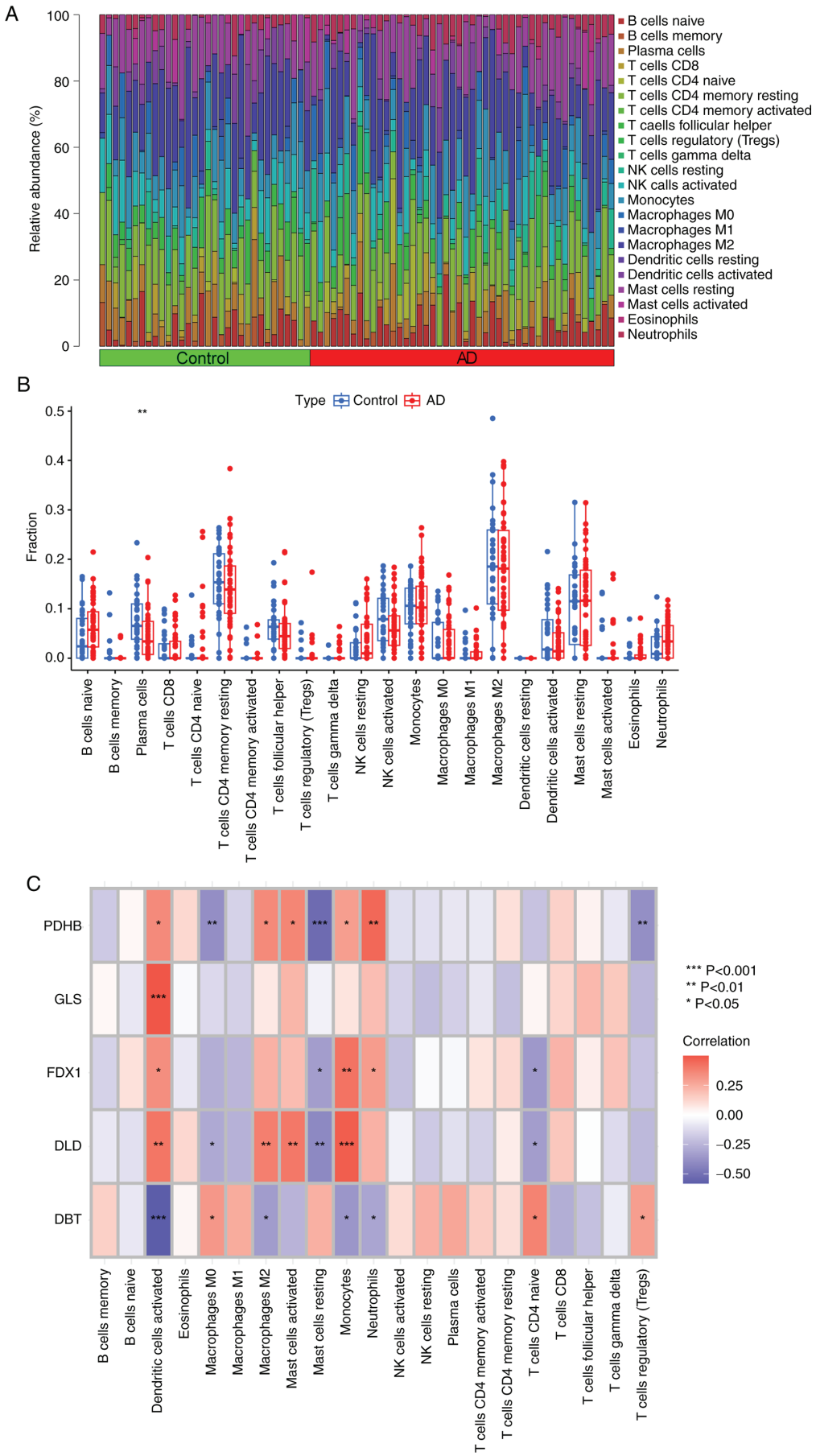

Figure 4. Immune infiltration analysis of CRGs. (A) Relative abundance of 22 infiltrating immune cells between AD and non-AD controls. (B) Difference in immune infiltration between AD and non-AD controls. (C) Correlation analysis of five differentially expressed CRGs with infiltrating immune cells. *P<0.05, **P<0.01 and ***P<0.001. AD, Alzheimer's disease; CRG, core cuproptosis genes; DLD, dihydrolipoamide dehydrogenase; FDX1, ferredoxin 1; GLS, glutaminase; PDHB, pyruvate dehydrogenase E1 subunit β; DBT, dihydrolipoamide branched chain transacylase E2.

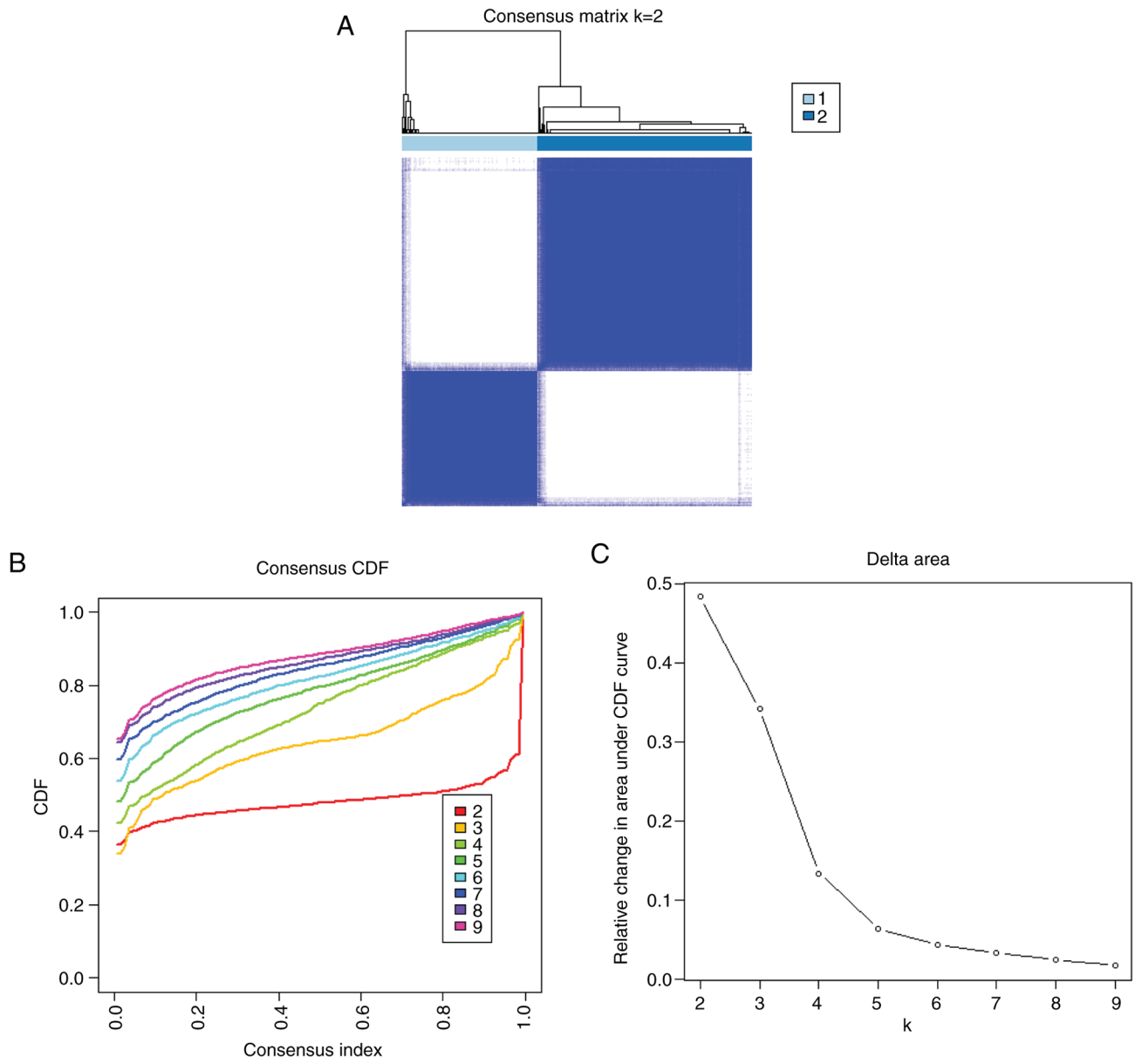

Figure 5. Identification of cuproptosis-related molecular clusters in AD. (A) Consistent clustering matrix when k=2. (B) CDF δ-area curve. (C) Consistency clustering score. AD, Alzheimer's disease; CDF, cumulative distribution function.

cancer, glycosaminoglycan biosynthesis of keratan sulfate, basal cell carcinoma, Kegel's chronic granulocytic leukemia, primary immunodeficiency, drug metabolism of cytochrome P450, isobiotic metabolism by cytochrome P450 and Notch signaling activity (Fig. 9B). Thus, AD may be associated with various immune responses and metabolism.

Development and evaluation of machine learning models. To identify specific genes with high diagnostic value, four validated machine learning models were developed based on the intersection of 134 cluster-specific DEGs and AD DEGs. These four models were RF, SVM, GLM and XGB. The SVM and RF models presented relatively low residuals (Fig. 10A and B). The top 15 significant feature variables of each model were then ranked based on the root mean square error (Fig. 10C). The discriminative performance of the four machine learning algorithms in the test dataset was evaluated by calculating the subject operating characteristic The discriminative performance of the four machine learning algorithms on the test dataset was evaluated by calculating the receiver operating characteristic (ROC) based on 5-fold cross-validation. The SVM showed the highest area under the ROC curve (AUC). The AUC of other models was as follows: GLM=0.585, SVM=0.803, RF=0.761 and XGB=0.624 (Fig. 10D). Combined with these results, the SVM was shown to distinguish well between patients belonging to different clusters. Finally, the top five SVM variables (CACNG3, TNS1, TCEAL2, FAM65C NPTN, and THY1) were selected as predictor genes for further analysis.

Nomogram construction and validation of predictive modeling accuracy. A nomogram was developed to estimate the risk of cuproptosis in 78 patients with AD to further generalize the RF model to clinical applications (Fig. 11A). Correction

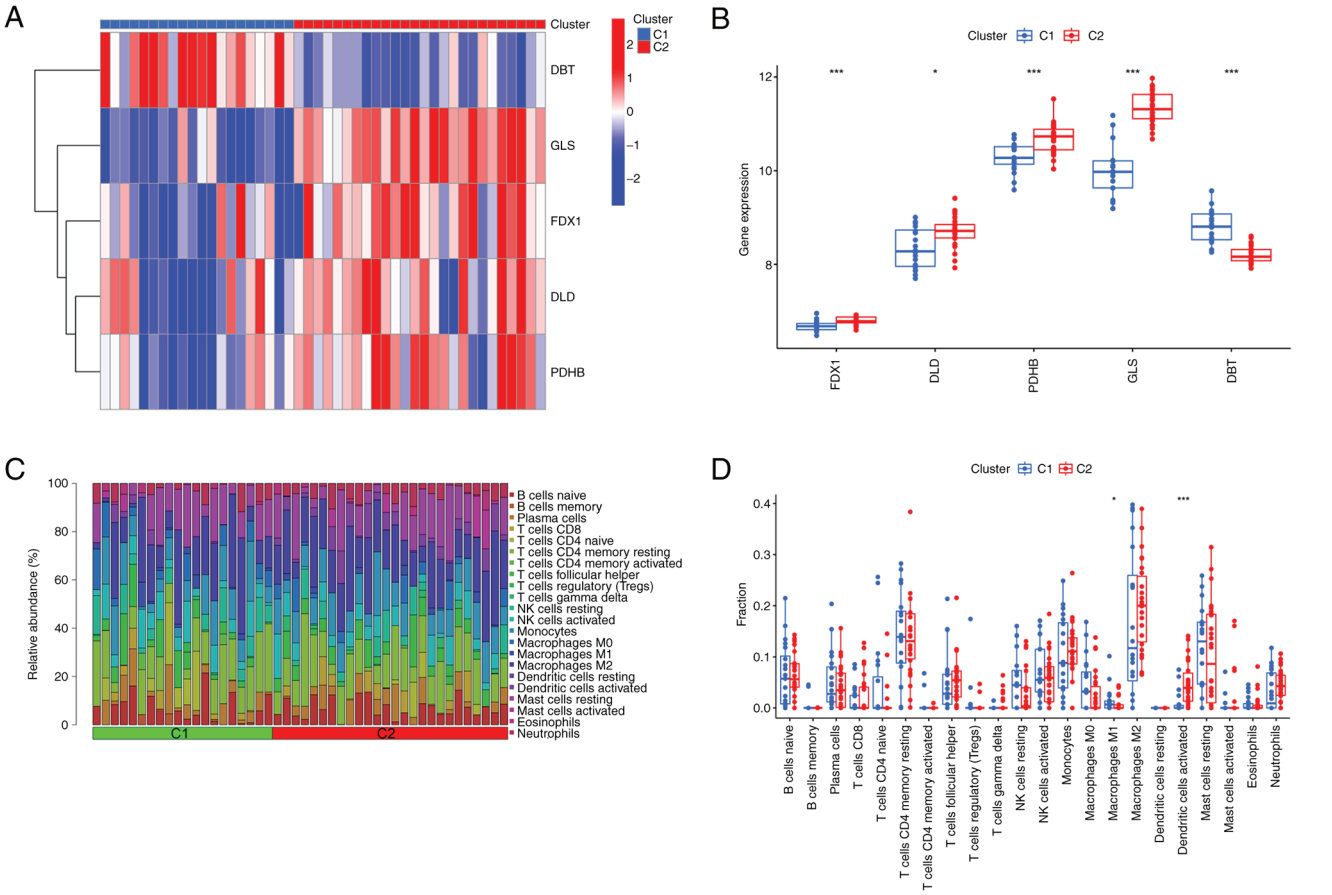

Figure 6. Identification of molecular and immunological features between the two clusters. (A) Clinical characterization of the five CRGs between the two clusters is presented in the heatmap. (B) Box plots showing the expression differences of individual CRGs between the two clusters. (C) Relative abundance of 22 infiltrating immune cells between the two cuproptosis clusters. (D) Difference in immune infiltration between two cuproptosis clusters. *P<0.05 and ***P<0.001. AD, Alzheimer's disease; CRG, core cuproptosis genes; DLD, dihydrolipoamide dehydrogenase; FDX1, ferredoxin 1; GLS, glutaminase; PDHB, pyruvate dehydrogenase E1 subunit β; DBT, dihydrolipoamide branched chain transacylase E2; C1, cluster 1; C2, cluster 2.

curves and DCA were then employed to evaluate the predictive efficiency of the nomogram model. The calibration curve showed that there was a small error difference between the actual AD aggregation risk and the predicted risk (Fig. 11B). As the calibration curve of the nomogram confirmed its high accuracy, it can be used as a basis for clinical decisions (Fig. 11C). The gene prediction model developed in the present study was validated on two external tissue datasets, and the ROC curves showed that it performed well in the GSE33000 dataset, with an AUC of 0.837 (Fig. 11D). These results suggest the diagnostic power of the prediction model.

Characterization of CRG expression in animal models of AD. After the MWM confirmed the modeling of the AD model group, hippocampal tissue was collected for RT-qPCR and western blotting experiments to verify CRG expression. No animals perished during the MWM after modeling ten rats in each group, and the analysis revealed that five modeling attempts were successful for the model group (n=5). The MWM was used to test the effect of $A\beta_{25-35}$ on cognitive function in SD rats. Fig. 12A shows the distance traveled by each group of rats in the MWM. The 4-day hidden platform experiment showed that rats in the AD group (treated with $A\beta_{25-35}$) had lower mean swimming speeds and longer escape latencies than the control and saline groups (Fig. 12B and C). The spatial exploration experiment also indicated that the rats in the model group traversed the platform less frequently than those in the control and saline groups (Fig. 12D). These results suggest that the memory function was impaired in the AD group. The RT-qPCR results showed that the relative expression of DLD, FDX1, GLS, and PDHB mRNA in the model group was lower than that in the control and saline groups, whereas the expression level of DBT mRNA in the model group was higher than that of the other two groups (Fig. 12E). Furthermore, the relative expression level of DLD, GLS, and PDHB proteins showed a reduction and that of DBT showed an increase in the model group compared with those in the control and saline groups (Fig. 12F and G). These results indicated that the expression of DLD, FDX1, GLS, and PDHB was downregulated and the expression of DBT was upregulated in the AD model group, which supports the bioinformatic analysis results.

Characterization of CRG expression in AD cell models. The modeling drug concentration of 25 nM was determined based on the IC_{50} value after OA action on SH-SY5Y cells at various concentrations was observed (Fig. 13A). A drug concentration of 25 nM was added to the cells for 24 h, and cell viability was determined to investigate the effects of this concentration on the cell proliferation rate (Fig. 13B). The AD model

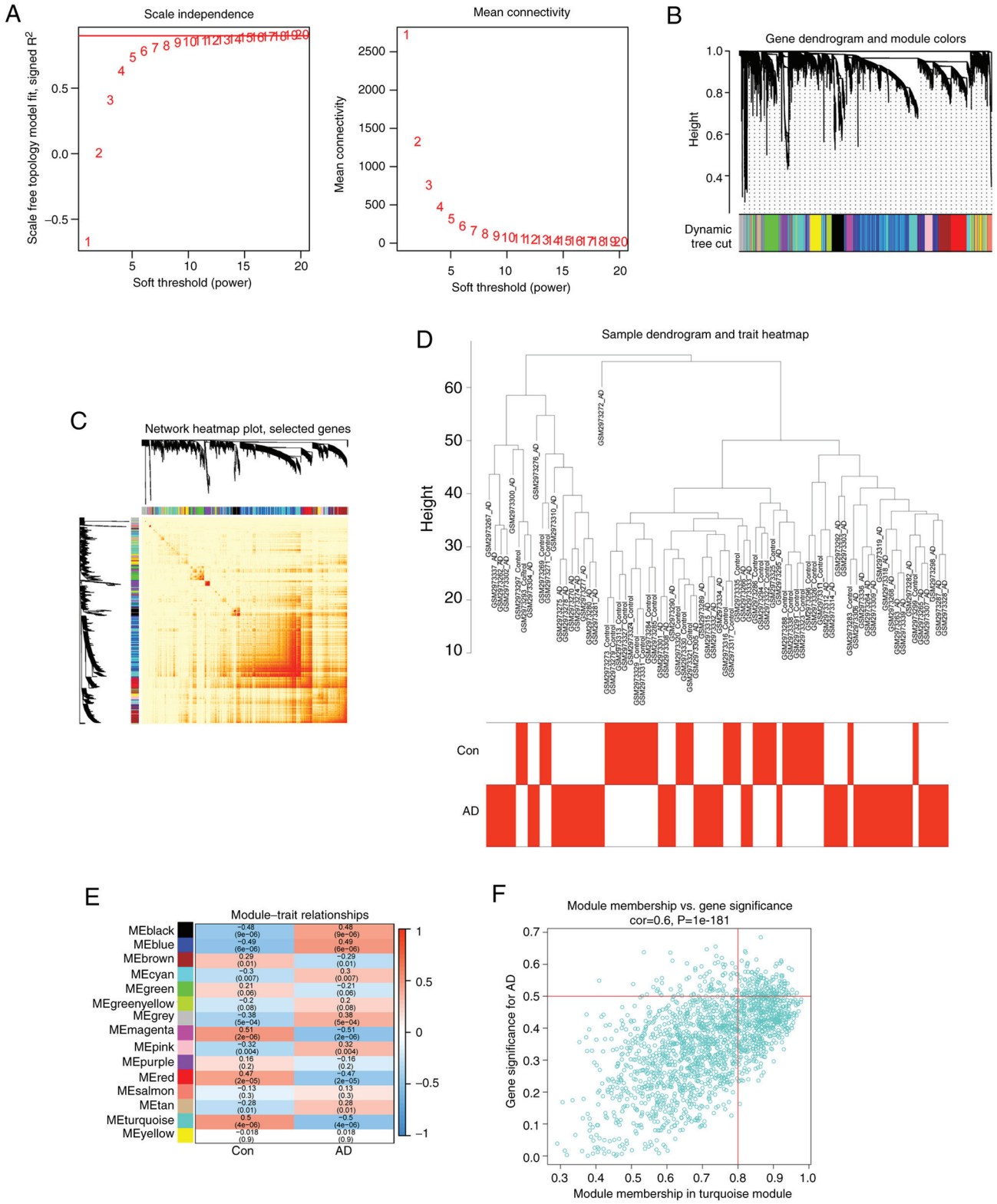

Figure 7. Co-expression network of differentially expressed genes in AD. (A) Selection of soft threshold power. (B) Cluster tree dendrogram of co-expression modules. Different colors represent different co-expression modules. (C) Representative heatmap of correlations between multiple modules. (D) Representative clustering of genes characterized by modules. (E) Correlation analysis of module feature genes with clinical status. Each row represents a module; each column represents clinical status. (F) Scatterplot between module membership associations in turquoise modules and gene significance for AD. Con, control; AD, Alzheimer's disease; cor, correlation.

was then created using this drug concentration. Based on the results of RT-qPCR, it was found that there was no statistically significant difference in mRNA expression levels between the normal control group and the DMSO group (Fig. 13C). According to the RT-qPCR results, the expression of DLD, FDX1, GLS and PDHB was lower and the expression of DBT was higher in the cells of the drug group than that of the normal group (Fig. 13D). Western blotting results also showed

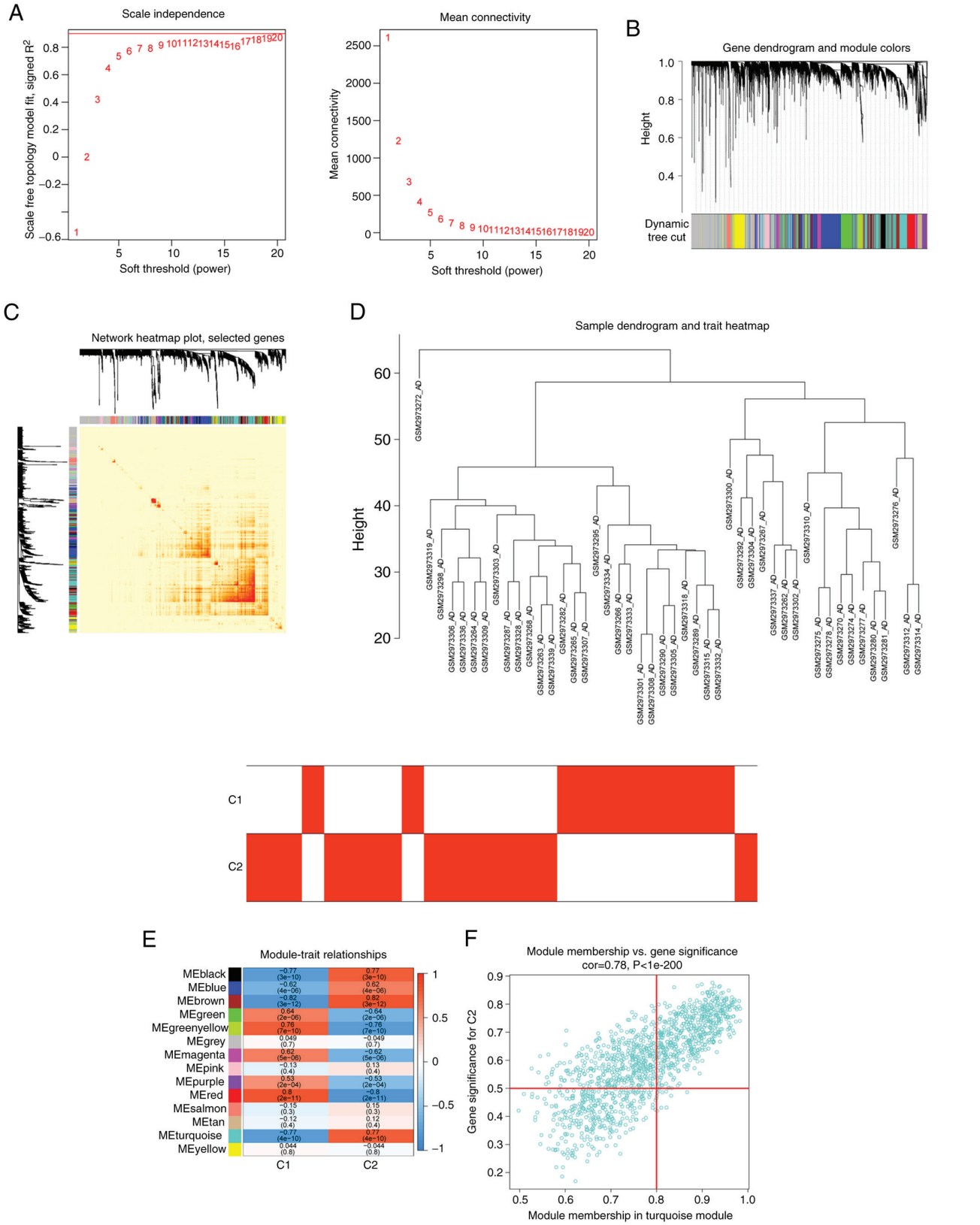

Figure 8. Co-expression network of differentially expressed genes between two cuproptosis clusters. (A) Selection of soft threshold power. (B) Cluster tree dendrogram of co-expression modules. Different colors represent different co-expression modules. (C) Clustering of genes representing module features. (D) Representative heatmap of correlations between multiple modules. (E) Correlation analysis of module feature genes with clinical status. Each row represents a module; each column represents clinical status. (F) Scatterplot between module membership associations in turquoise modules and gene significance in cluster 2. Con, control; AD, Alzheimer's disease; cor, correlation; C2, cluster 2.

that the DLD, GLS and PDHB content decreased and the DBT content increased in the drug group (Fig. 13E and F). These findings support the results of the bioinformatics analysis and the animal model.

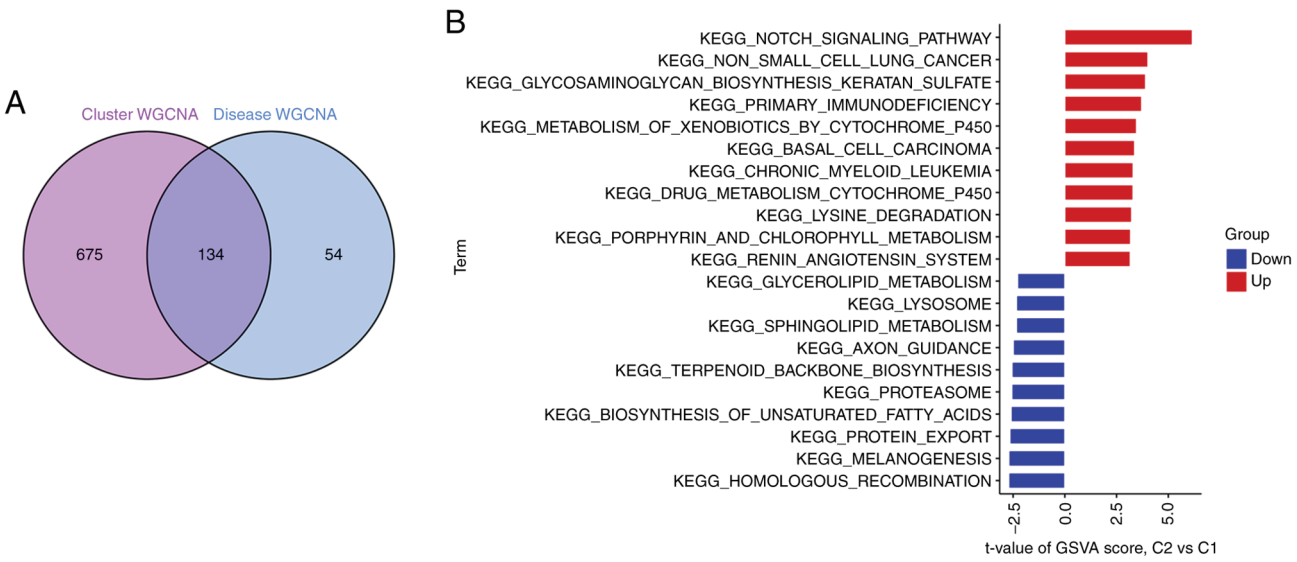

Figure 9. Identification of DEGs specific between two cuproptosis clusters and their biological characterization. (A) Cross-over between module-associated genes dying in copper and module-associated genes in the GSE109887 dataset. (B) Differences in marker pathway activity between Cluster 1 and 2 samples were sorted by the t-value of the GSVA method. DEGs, differentially expressed genes; GSVA, gene set variation analysis; WGCNA, weighted gene co-expression network analysis; C1, cluster 1; C2, cluster 2.

Discussion

The pathogenesis and pathologic characteristics of AD are complex. Apart from the primary pathological characteristics such as NFTs, SPs and neuronal loss, patients with AD also exhibit signs of mitochondrial dysfunction, including altered mitochondrial morphology, decreased activity of cytochrome oxidase (respiratory chain complex IV) and decreased glucose metabolism (35). Metal ions can cause neurodegeneration in patients with AD by disrupting the mitochondrial functional cycle, which has been suggested to be closely associated with mitochondrial respiration by cuproptosis ions and cuproptosis, a type of cell death with cuproptosis dependence (16,36). Since cuproptosis ions induce Aβ aggregation and the generation of reactive oxygen species, they may play a role in the progression of AD (37). For example, Aβ aggregation-mediated oxidative stress leads to mitochondrial dysfunction and accelerates the progression of AD (38,39). Zhang *et al* (40) suggested that cuproptosis-activated oxidative stress may affect memory function in patients with AD. The findings of Pilozzi *et al* (41) also verified the effects of cuproptosis redox on AD amyloid pathology. There is a close association between AD and cuproptosis in mitochondrial function and the oxidative respiratory chain (42). This is consistent with the enrichment analysis results in the present study. For example, GO and KEGG analyses showed that CRGs, such as FDX1, DLD and PDHB, are closely associated to the oxidative respiratory chain and play a role in mitochondrial functions. This is consistent with the findings of Starkov *et al* (43) and Yang *et al* (44). Therefore, it can be hypothesized that there are similarities between the mechanisms of AD and cuproptosis. However, few studies have explored the association between cuproptosis and AD, and the mechanisms involved are still unclear. Therefore, the specific roles of CRGs in AD development and the immune microenvironment were explored in the present study to develop a prognostic risk model for AD through machine learning.

It has been shown that immune cells in the human brain, such as microglia and astrocytes, are involved in AD pathogenesis (45). Several studies have investigated the effects of cuproptosis ions and cuproptosis on the infiltration of immune cells (46,47). The correlation analysis of CRGs of infiltrating immune cells in the present study showed that almost all genes were strongly associated with dendritic cell activation and monocytes. Other studies have also proven the significantly higher infiltration of primitive B cells and neutrophils in the hippocampus of patients with AD (48,49). Subsequent experiments revealed the high similarity between DLD and PDHB in the infiltration of immune cells, supporting the strong positive association between these two variables, as shown by the correlation analysis.

The interactions of various computational biology fields are prominent in disease prediction research, and there are numerous machine learning algorithms available today for disease clinical trait analysis (50). For example, DMFGAM is a novel deep learning prediction model that performs well in disease drug discovery prediction and this model is expected to introduce new targets for AD drug development due to the failure of clinical trials involving multiple drugs targeting the disease (51,52). Additionally, some research has indicated that by examining the mechanism of action of non-coding RNAs in AD (53), as well as the recently proposed computational model GCNCRF, which is based on graph convolutional neural networks and conditional random fields in the model (54), it is anticipated to create a new avenue for AD diagnosis and treatment. It can predict human lncRNA-miRNA interactions more accurately by grasping the feature information of important nodes (55). This shows the importance of machine learning algorithms in disease prediction. The present study compared four selected machine learning classifiers (RF, SVM, GLM and XGB) and verified that the SVM model had a higher prediction accuracy through a more precise multifactor analysis.

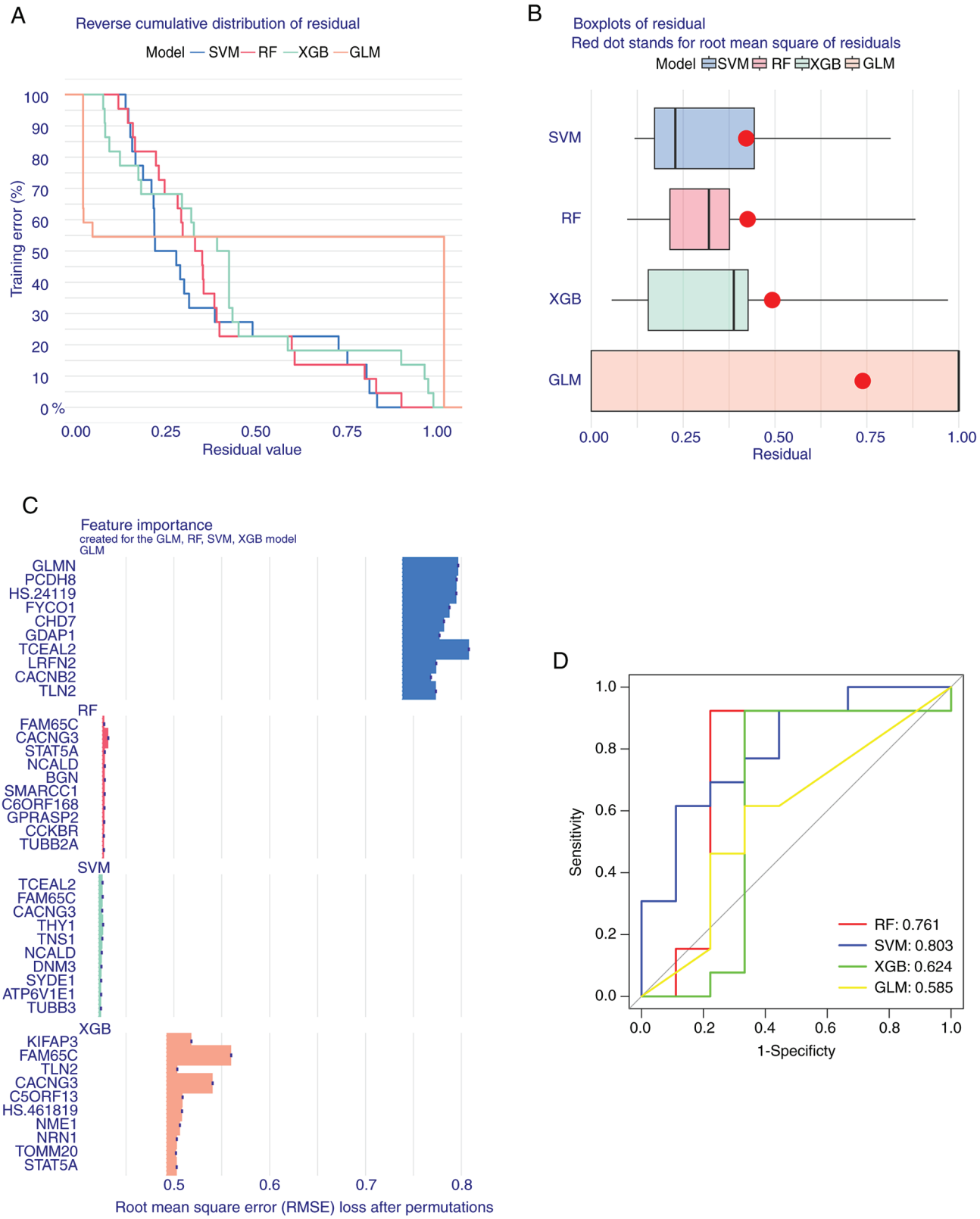

Figure 10. Construction of RF, SVM, GLM and XGB machine models. (A) Cumulative residual distribution for each machine learning model. (B) Box plots showing the residuals for each machine learning model. The red dots indicate the root mean square of the residuals. (C) Important features in RF, SVM, GLM and XGB machine models. (D) ROC analysis of the four machine learning models based on 5-fold cross-validation in the test cohort. RF, Random Forest Model; SVM, Support Vector Machine Model; GLM, Generalized Linear Model; XGB, Extreme Gradient Boosting.

The present study results confirmed the acceptable diagnostic power of the AD risk prediction model developed based on five cuproptosis genes (including DLD, FDX1, GLS, PDHB and DBT). The FDX1 gene promotes lipoylation of pyruvate dehydrogenase and α-ketoglutarate dehydrogenase, which in turn affects the TCA cycle; decreased expression of FDX1

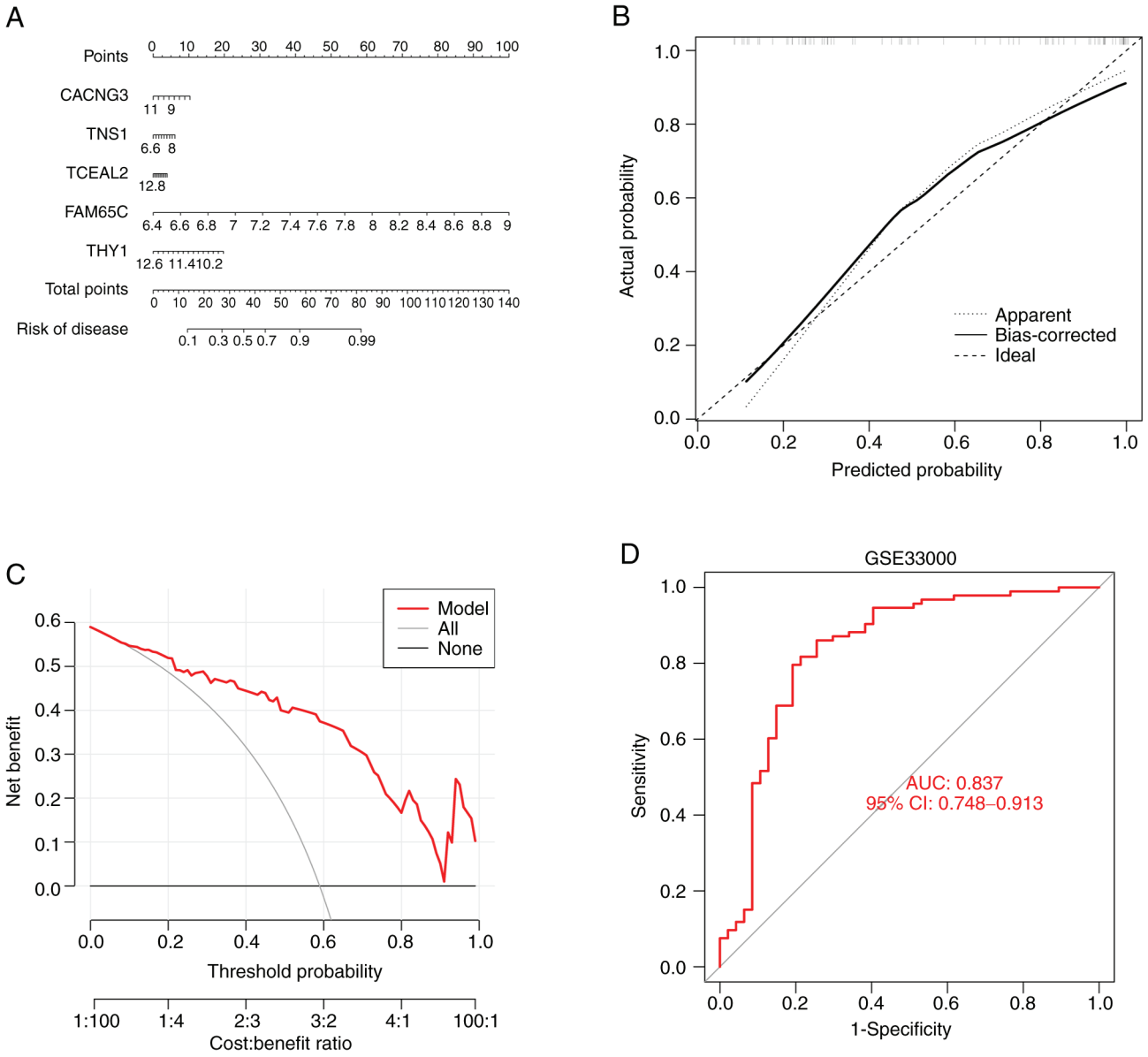

Figure 11. Validation of SVM models. (A) Nomogram of 5-gene-based SVM models constructed for predicting risk of AD clusters. (B) Calibration curves to assess the predictive effectiveness of scaled plots. (C) Predictive efficiency of the column-line graph model used to assess the predictive efficiency of the column-line graph model. (D) ROC analysis of a 5-gene-based SVM model based on 5-fold cross-validation in GSE33000. SVM, Support Vector Machine Model; AD, Alzheimer's disease; DCA, decision curve analysis; ROC, receiver operating characteristic; CI, confidence interval.

promotes mitochondrial TCA cycling (56). By contrast, the PDHB gene and the DLD gene are involved in encoding the pyruvate dehydrogenase complex, which is essential for mitochondrial respiration (57) and is also closely associated with the regulation of FDX1 and AD (58,59). The branched-chain α-ketoacid dehydrogenase complex is an endomitochondrial enzyme complex that influences the catabolism of the branched-chain amino acids isoleucine, leucine and valine, and it has been closely linked to the pathogenesis of AD (60). The DBT gene encoding the transacylase E2 subunit is also involved in the formation of this complex (60). By contrast, the GLS gene, an ammonia metabolism gene, has been reported to be associated with a wide range of glutamate signaling disorders, including AD (61). In the present study, significant differences in the expression levels of DLD, FDX1, GLS, DBT and PDHB were found between the AD group and the normal group. The results showed an increase in DBT expression, and a decrease in DLD, FDX1, GLS and PDHB expression in the AD group. The difference between cluster 1 and 2 in the marker pathway activity also revealed a significant increase in Notch signaling pathway activity. Kapoor *et al* (62) and Perna *et al* (63) also reported an association between the Notch signaling pathway and AD. The present study validated the accuracy of a machine learning model developed based on CRGs using an external dataset, GSE33000, and developed a nomogram for assessing AD risk using CRG scores. Calibration curves and DCA confirmed the accuracy of the model.

The present study had several limitations. Firstly, it was challenging to conduct additional analyses due to the small sample size of the dataset and the number of patients with AD available for analysis selection. More clinical trait data are required in order to further validate the results of the

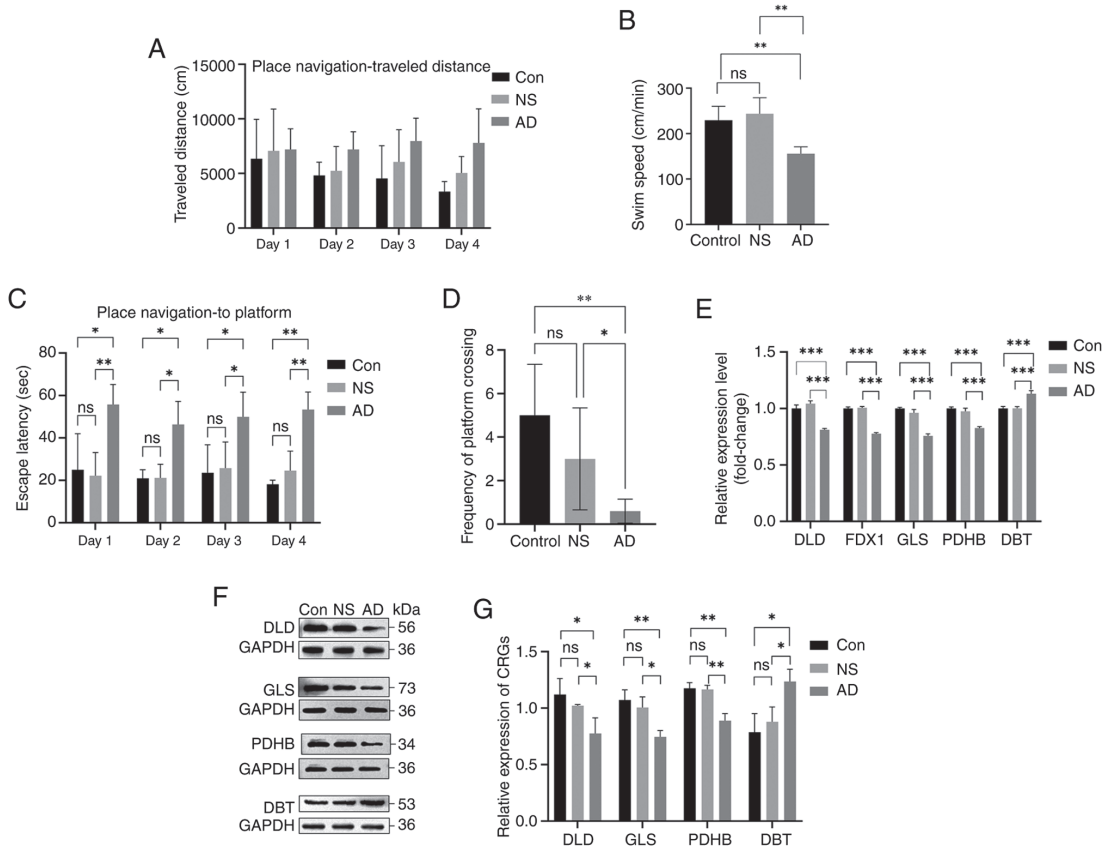

Figure 12. Validation of the animal model (n=5 animals/group; experiments repeated three times). (A) Distance travelled during spatial training. (B) Swimming speed during the search for the MWM platform. (C) Escape latency in the MWM experiment. (D) Frequency of platform crossing in the exploration experiment. (E) mRNA levels of DLD, FDX1, GLS, PDHB and DBT in the hippocampus of rats in each group. (F) Protein expression levels of DLD, GLS, PDHB and DBT in the hippocampus of rats in each group. (G) Protein expression levels of cuproptosis-related genes in control and AD groups. *P<0.05, **P<0.01, ***P<0.001. ns, not significant; MWM, Morris water maze; DLD, dihydrolipoamide dehydrogenase; FDX1, ferredoxin 1; GLS, glutaminase; PDHB, pyruvate dehydrogenase E1 subunit β; DBT, dihydrolipoamide branched chain transacylase E2; AD, Alzheimer's disease; Con, control; NS, normal saline.

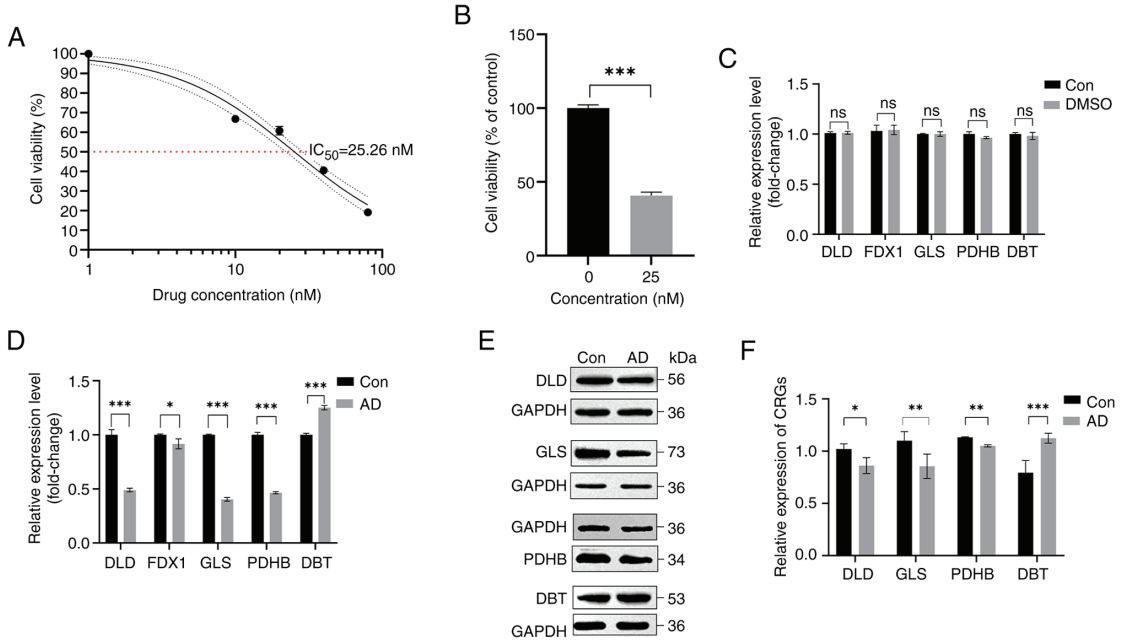

Figure 13. Validation of cell models. (A) Calculated IC_{50} results at 0, 10, 20, 40 and 80 nM okadaic acid concentrations. (B) Cell viability of 25 nM okadaic acid drug concentration acting on cells for 24 h. (C) mRNA levels of DLD, FDX1, GLS, PDHB and DBT in control and DMSO groups. (D) mRNA levels of DLD, FDX1, GLS, PDHB and DBT in control and model groups. (E) Protein expression levels of DLD, GLS, PDHB and DBT in SH-SY5Y cells of the AD model group. (F) Protein expression levels of cuproptosis-related genes in control, NS and AD groups. *P<0.05, **P<0.01 and ***P<0.001. ns, not significant; Con, control; DLD, dihydrolipoamide dehydrogenase; FDX1, ferredoxin 1; GLS, glutaminase; PDHB, pyruvate dehydrogenase E1 subunit β; DBT, dihydrolipoamide branched chain transacylase E2; AD, Alzheimer's disease.

bioinformatics analysis. Secondly, the present study demonstrated a correlation between cuproptosis and AD, but no further investigation was carried out to validate the precise mechanism underlying the role of related DEGs in AD. In addition, the use of machine learning algorithms in the present study was limited to the analysis of clinical traits, and no further in-depth studies, such as drug screening, were conducted. Therefore, further algorithm updates are needed in the future.

The present study investigated the complex association between cuproptosis and AD by identifying five core cuproptosis genes (DLD, FDX1, GLS, PDHB and DBT) associated with AD. The *in vivo* and *in vitro* experiments also validated the expression level of these five core cuproptosis genes in AD models. The present study demonstrated the association between CRGs and infiltrating immune cells. In addition, a practical prognostic risk model was developed to assess the risk of cuproptosis and the pathological consequences of AD. The association between the five core cuproptosis genes and AD was validated by multiple data analyses and *in vivo* and *ex vivo* experiments. The present study results revealed the downregulation of DLD, FDX1, GLS and PDHB and the upregulation of DBT in patients with AD, compared with healthy individuals. This differential expression is expected to provide new ideas for the diagnosis and prognostic monitoring of AD.

Acknowledgements

Not applicable.

Funding

The present study was funded by the Project of Enhancement of Basic Research Ability of Young and Middle-aged Teachers in Guangxi Universities (grant no. 2023KY0554) and the Baise City Science and Technology Program Project (grant nos. 20211807 and 20224139).

Availability of data and materials

The data generated in the present study may be requested from the corresponding author.

Authors' contributions

RH conducted the validation experiments and collected the experimental data, and collaborated with ZX on the statistical analysis and paper writing. MYQ, CYL, GYW and YYW assisted in the animal feeding and sampling process. ZSH and MYD participated in the conceptualization of the whole article, revised the manuscript and participated in the technical support. RH, ZH, MYD and ZSH confirm the authenticity of all raw data. All authors read and approved the final version of the manuscript.

Ethics approval and consent to participate

The present study received ethical approval for the use of experimental animals from Youjiang Medical University For Nationalities (Baise, China; approval no. 2023040101).

Patient consent for publication

Not applicable.

Competing interests

The authors declare that they have no competing interests.

References

1. de San Román EG, Manuel I, Giralt MT, Ferrer I and Rodríguez-Puertas R: Imaging mass spectrometry (IMS) of cortical lipids from preclinical to severe stages of Alzheimer's disease. Biochim Biophys Acta Biomembr 1859(9 Pt B): 1604-1614, 2017.
2. GBD 2019 Dementia Forecasting Collaborators: Estimation of the global prevalence of dementia in 2019 and forecasted prevalence in 2050: An analysis for the global burden of disease study 2019. Lancet Public health 7: e105-e125, 2022.
3. Rostagno AA: Pathogenesis of Alzheimer's disease. Int J Mol Sci 24: 107, 2022.
4. Chen YG: Research progress in the pathogenesis of Alzheimer's disease. Chin Med J (Engl) 131: 1618-1624, 2018.
5. Di Fede G, Catania M, Maderna E, Ghidoni R, Benussi L, Tonoli E, Giaccone G, Moda F, Paterlini A, Campagnani I, *et al*: Molecular subtypes of Alzheimer's disease. Sci Rep 8: 3269, 2018.
6. Scheltens P, De Strooper B, Kivipelto M, Holstege H, Chételat G, Teunissen CE, Cummings J and van der Flier WM: Alzheimer's disease. Lancet 397: 1577-1590, 2021.
7. Sanchez-Mut JV and Gräff J: Epigenetic alterations in Alzheimer's disease. Front Behav Neurosci 9: 347, 2015.
8. Kawamata H and Manfredi G: Import, maturation, and function of SOD1 and its copper chaperone CCS in the mitochondrial intermembrane space. Antioxid Redox Signal 13: 1375-1384, 2010.
9. Scheiber I, Dringen R and Mercer JF: Copper: Effects of deficiency and overload. Met Ions Life Sci 13: 359-387, 2013.
10. Gromadzka G, Tarnacka B, Flaga A and Adamczyk A: Copper dyshomeostasis in neurodegenerative diseases-therapeutic implications. Int J Mol Sci 21: 9259, 2020.
11. Sayre LM, Perry G, Harris PL, Liu Y, Schubert KA and Smith MA: In situ oxidative catalysis by neurofibrillary tangles and senile plaques in Alzheimer's disease: A central role for bound transition metals. J Neurochem 74: 270-279, 2000.
12. Chen LL, Fan YG, Zhao LX, Zhang Q and Wang ZY: The metal ion hypothesis of Alzheimer's disease and the anti-neuroinflammatory effect of metal chelators. Bioorg Chem 131: 106301, 2023.
13. Tang D, Chen X and Kroemer G: Cuproptosis: A copper-triggered modality of mitochondrial cell death. Cell Res 32: 417-418, 2022.
14. Garza NM, Swaminathan AB, Maremanda KP, Zulkifli M and Gohil VM: Mitochondrial copper in human genetic disorders. Trends Endocrinol Metab 34: 21-33, 2023.
15. Tsvetkov P, Coy S, Petrova B, Dreishpoon M, Verma A, Abdusamad M, Rossen J, Joesch-Cohen L, Humeidi R, Spangler RD, *et al*: Copper induces cell death by targeting lipoylated TCA cycle proteins. Science 375: 1254-1261, 2022.
16. Xie J, Yang Y, Gao Y and He J: Cuproptosis: Mechanisms and links with cancers. Mol Cancer 22: 46, 2023.
17. Swerdlow RH: Mitochondria and mitochondrial cascades in Alzheimer's disease. J Alzheimers Dis 62: 1403-1416, 2018.
18. Macdonald R, Barnes K, Hastings C and Mortiboys H: Mitochondrial abnormalities in Parkinson's disease and Alzheimer's disease: Can mitochondria be targeted therapeutically? Biochem Soc Trans 46: 891-909, 2018.
19. Nie B, Duan Y, Xie X, Qiu L, Shi S, Fan Z, Zheng X and Jiang L: Systematic analysis of cuproptosis-related genes in immunological characterization and predictive drugs in Alzheimer's disease. Front Aging Neurosci 15: 1204530, 2023.
20. Li R: Data mining and machine learning methods for dementia research. Methods Mol Biol 1750: 363-370, 2018.
21. Duffy IR, Boyle AJ and Vasdev N: Improving PET imaging acquisition and analysis with machine learning: A narrative review with focus on Alzheimer's disease and oncology. Mol Imaging 18: 1536012119869070, 2019.

22. Lardenoije R, Roubroeks JAY, Pishva E, Leber M, Wagner H, Iatrou A, Smith AR, Smith RG, Eijssen LMT, Kleineidam L, *et al*: Alzheimer's disease-associated (hydroxy)methylomic changes in the brain and blood. Clin Epigenetics 11: 164, 2019.
23. Narayanan M, Huynh JL, Wang K, Yang X, Yoo S, McElwee J, Zhang B, Zhang C, Lamb JR, Xie T, *et al*: Common dysregulation network in the human prefrontal cortex underlies two neurodegenerative diseases. Mol Syst Biol 10: 743, 2014.
24. Kanehisa M, Furumichi M, Sato Y, Kawashima M and Ishiguro-Watanabe M: KEGG for taxonomy-based analysis of pathways and genomes. Nucleic Acids Res 51(D1): D587-D592, 2023.
25. Ritchie ME, Phipson B, Wu D, Hu Y, Law CW, Shi W and Smyth GK: limma powers differential expression analyses for RNA-sequencing and microarray studies. Nucleic Acids Res 43: e47, 2015.
26. Varma S: Blind estimation and correction of microarray batch effect. PLoS One 15: e0231446, 2020.
27. Newman AM, Liu CL, Green MR, Gentles AJ, Feng W, Xu Y, Hoang CD, Diehn M and Alizadeh AA: Robust enumeration of cell subsets from tissue expression profiles. Nat Methods 12: 453-457, 2015.
28. Hänzelmann S, Castelo R and Guinney J: GSVA: Gene set variation analysis for microarray and RNA-seq data. BMC Bioinformatics 14: 7, 2013.
29. My S, Lazareva NA, Onufriev MV, Mitrokhina OS, YuV M and Gulyaeva NV: Effects of doses of fragment (25-35) of beta-amyloid peptide on behavior in rats. Neurosci Behav Physiol 28: 564-566, 1998.
30. Li Z, Tong Q, Xu H, Hu L, Zhao R, Zhou F, Pan W and Zhou L: Therapeutic effects of TianDiJingWan on the Aβ 25-35-induced Alzheimer's disease model rats. Evid Based Complement Alternat Med 2015: 307350, 2015.
31. Othman MZ, Hassan Z and Has AT: Morris water maze: A versatile and pertinent tool for assessing spatial learning and memory. Exp Anim 71: 264-280, 2022.
32. Livak KJ and Schmittgen TD: Analysis of relative gene expression data using real-time quantitative PCR and the 2(-Delta Delta C(T)) method. Methods 25: 402-408, 2001.
33. Amonruttanapun P, Chongthammakun S and Chamniansawat S: The effects of okadaic acid-treated SH-SY5Y cells on microglia activation and phagocytosis. Cell Biol Int 46: 234-242, 2022.
34. Yang X, Zhong Y, Wang D and Lu Z: A simple colorimetric method for viable bacteria detection based on cell counting Kit-8. Anal Methods 13: 5211-5215, 2021.
35. Zhu X, Smith MA, Perry G and Aliev G: Mitochondrial failures in Alzheimer's disease. Am J Alzheimers Dis Other Demen 19: 345-352, 2004.
36. Mezzaroba L, Alfieri DF, Simão AN and Reiche EM: The role of zinc, copper, manganese and iron in neurodegenerative diseases. Neurotoxicology 74: 230-241, 2019.
37. Hureau C and Faller P: Abeta-mediated ROS production by Cu ions: Structural insights, mechanisms and relevance to Alzheimer's disease. Biochimie 91: 1212-1217, 2009.
38. Butterfield DA and Boyd-Kimball D: Redox proteomics and amyloid β-peptide: Insights into Alzheimer disease. J Neurochem 151: 459-487, 2019.
39. Jansen IE, van der Lee SJ, Gomez-Fonseca D, de Rojas I, Dalmasso MC, Grenier-Boley B, Zettergren A, Mishra A, Ali M, Andrade V, *et al*: Genome-wide meta-analysis for Alzheimer's disease cerebrospinal fluid biomarkers. Acta Neuropathol 144: 821-842, 2022.
40. Zhang Y, Zhou Q, Lu L, Su Y, Shi W, Zhang H, Liu R, Pu Y and Yin L: Copper induces cognitive impairment in mice via modulation of cuproptosis and CREB signaling. Nutrients 15: 972, 2023.
41. Pilozzi A, Yu Z, Carreras I, Cormier K, Hartley D, Rogers J, Dedeoglu A and Huang X: A preliminary study of Cu exposure effects upon Alzheimer's amyloid pathology. Biomolecules 10: 408, 2020.
42. Huang X: A concise review on oxidative stress-mediated ferroptosis and cuproptosis in Alzheimer's disease. Cells 12: 1369, 2023.
43. Starkov AA, Fiskum G, Chinopoulos C, Lorenzo BJ, Browne SE, Patel MS and Beal MF: Mitochondrial alpha-ketoglutarate dehydrogenase complex generates reactive oxygen species. J Neurosci 24: 7779-7788, 2004.
44. Yang W, Guo Q, Wu H, Tong L, Xiao J, Wang Y, Liu R, Xu L, Yan H and Sun Z: Comprehensive analysis of the cuproptosis-related gene DLD across cancers: A potential prognostic and immunotherapeutic target. Front Pharmacol 14: 1111462, 2023.
45. Rajesh Y and Kanneganti TD: Innate immune cell death in neuroinflammation and Alzheimer's disease. Cells 11: 1885, 2022.
46. Suliman IH, Kim K, Chen W, Kim Y, Moon JH, Son S and Nam J: Metal-based nanoparticles for cancer metalloimmunotherapy. Pharmaceutics 15: 2003, 2023.
47. Wang L, Cao Y, Guo W and Xu J: High expression of cuproptosis-related gene FDX1 in relation to good prognosis and immune cells infiltration in colon adenocarcinoma (COAD). J Cancer Res Clin Oncol 149: 15-24, 2023.
48. Huang LT, Zhang CP, Wang YB and Wang JH: Association of peripheral blood cell profile with Alzheimer's disease: A meta-analysis. Front Aging Neurosci 14: 888946, 2022.
49. Song L, Yang YT and Guo Q; ZIB Consortium; Zhao XM: Cellular transcriptional alterations of peripheral blood in Alzheimer's disease. BMC Med 20: 266, 2022.
50. Waschkies KF, Soch J, Darna M, Richter A, Altenstein S, Beyle A, Brosseron F, Buchholz F, Butryn M, Dobisch L, *et al*: Machine learning-based classification of Alzheimer's disease and its at-risk states using personality traits, anxiety, and depression. Int J Geriatr Psychiatry 38: e6007, 2023.
51. Wang T, Sun J and Zhao Q: Investigating cardiotoxicity related with hERG channel blockers using molecular fingerprints and graph attention mechanism. Comput Biol Med 153: 106464, 2023.
52. Becker RE and Greig NH: Why so few drugs for Alzheimer's disease? Are methods failing drugs?. Curr Alzheimer Res 7: 642-651, 2010.
53. Li L, Jin M, Tan J and Xiao B: NcRNAs: A synergistically anti-apoptosis therapeutic tool in Alzheimer's disease. CNS Neurosci Ther 30: e14476, 2023.
54. Wang W, Zhang L, Sun J, Zhao Q and Shuai J: Predicting the potential human lncRNA-miRNA interactions based on graph convolution network with conditional random field. Brief Bioinform 23: bbac463, 2022.
55. Zhao J, Sun J, Shuai SC, Zhao Q and Shuai J: Predicting potential interactions between lncRNAs and proteins via combined graph auto-encoder methods. Brief Bioinform 24: bbac527, 2023.
56. Dreishpoon MB, Bick NR, Petrova B, Warui DM, Cameron A, Booker SJ, Kanarek N, Golub TR and Tsvetkov P: FDX1 regulates cellular protein lipoylation through direct binding to LIAS. bioRxiv: The preprint server for biology, 2023.02.03.526472.
57. Patel MS, Nemeria NS, Furey W and Jordan F: The pyruvate dehydrogenase complexes: Structure-based function and regulation. J Biol Chem 289: 16615-16623, 2014.
58. Dreishpoon MB, Bick NR, Petrova B, Warui DM, Cameron A, Booker SJ, Kanarek N, Golub TR and Tsvetkov P: FDX1 regulates cellular protein lipoylation through direct binding to LIAS. J Biol Chem 299: 105046, 2023.
59. Chen Z and Zhong C: Decoding Alzheimer's disease from perturbed cerebral glucose metabolism: Implications for diagnostic and therapeutic strategies. Prog Neurobiol 108: 21-43, 2013.
60. Hull J, Moraes MU, Brookes E, Love S and Conway ME: Distribution of the branched-chain α-ketoacid dehydrogenase complex E1α subunit and glutamate dehydrogenase in the human brain and their role in neuro-metabolism. Neurochem Int 112: 49-58, 2018.
61. Griffin JWD, Liu Y, Bradshaw PC and Wang K: In silico preliminary association of ammonia metabolism genes GLS, CPS1, and GLUL with risk of Alzheimer's disease, major depressive disorder, and type 2 diabetes. J Mol Neurosci 64: 385-396, 2018.
62. Kapoor A and Nation DA: Role of Notch signaling in neurovascular aging and Alzheimer's disease. Semin Cell Dev Biol 116: 90-97, 2021.
63. Perna A, Marathe S, Dreos R, Falquet L, Egger HA and Auber LA: Revealing NOTCH-dependencies in synaptic targets associated with Alzheimer's disease. Mol Cell Neurosci 115: 103657, 2021.